Beam Frame Representation for Ultrawideband Radiation From Volume Source Distributions: Frequency-Domain and Time-Domain Formulations

Ram Tuvi, Ehud Heyman, *Life Fellow, IEEE*, and Timor Melamed, *Senior Member, IEEE*

***Abstract*— We present two novel beam-summation schemes for radiation from time-harmonic or time-dependent volume source distributions, where the field is expanded using a discrete phase-space set of beam-wave propagators. The generic term "beams" is used here for both the frequency-domain and the time-domain formulations where the propagators are isodiffracting Gaussian beam or isodiffracting pulsed beams, respectively. The formulations are structured upon the recently formulated "beam-frame" theorem that establishes these phase-space beam sets as frame sets everywhere in the propagation domain and not only over the aperture plane as in previous formulations. The expansion coefficients are obtained by projecting the source distributions over the dual beam-frame sets that have essentially the same structure as the basic sets. As such, these formulations constitute local generalization to the conventional plane waves or Green's function formulations, and also reduce the overall degrees of freedom needed to describe the radiated field. As demonstrated by the numerical examples, they resolve the local features of the source distributions in space time, and hence provide a basis for a new local inverse scattering theory to be presented subsequently.**

***Index Terms*— Beam-summation (BS) methods, Gaussian beams (GB), phase-space representations, pulsed beams (PB), radiation theory, time domain (TD), ultrawideband (UWB).**

Nomenclature

UWB	Ultrawideband.
GB	Gaussian beam.
PB	Pulsed beam.
ID	Isodiffracting.
FD	Frequency domain.
TD	Time domain.
WFT	Windowed Fourier Transform.
WRT	Windowed Radon transform.
BF	Beam frame.
PBF	PB frame.
UWB-PS-BS	UWB phase-space beam-summation method.
PS-PBS	Phase-space PB summation method.

Manuscript received April 14, 2018; revised August 15, 2018; accepted September 26, 2018. Date of publication November 20, 2018; date of current version February 5, 2019. This work was supported by Israeli Science Foundation under Grant 412/15. *(Corresponding author: Ehud Heyman.)*

R. Tuvi and E. Heyman are with the School of Electrical Engineering, Tel Aviv University, Tel Aviv 69978, Israel (e-mail: ram.tuvi@gmail.com; heyman@tau.ac.il).

T. Melamed is with the Department of Electrical and Computer Engineering, Ben-Gurion University of the Negev, Beer-Sheva 8410501, Israel (e-mail: timormel@bgu.ac.il).

Color versions of one or more of the figures in this paper are available online at http://ieeexplore.ieee.org.

Digital Object Identifier 10.1109/TAP.2018.2882219

I. Introduction

BEAM-summation (BS) methods have long been utilized for modeling wave propagation in complex environments due to their unique properties, combining: 1) local resolution of the (real or induced) source distributions; 2) asymptotically uniform spectral representation; and 3) algorithmic ray-based structure. We use the generic term "beams" for both FD and TD formulations where the propagators are ID-GB or ID-PB, respectively.

Several schemes for expanding time-harmonic or time-dependent source-excited fields in terms of a spectrum of beam waves have been introduced in the past (see a review in [1]). This paper is related to the UWB-PS-BS that has been introduced originally in the context of radiation from an aperture-source distribution [2]. In the UWB-PS-BS, the field is expanded using an overcomplete phase-space set of GBs that emanate from a discrete set of points and directions over the aperture. As such, this method is related to the Gabor-series expansion [3]–[6]. The main drawbacks of the Gabor series are the coefficients instability, even at a single frequency, and the fact that the beam lattice needs to be recalculate for each frequency [7], rendering the method inapplicable for UWB applications. These obstacles were removed in the UWB-PS-BS which is structured on Gabor frame (also termed WFT frame). Here, the frame overcompleteness has been used in a unique fashion that renders the beams' trajectories and their propagation parameters *frequency independent*. Thus, the beam set is calculated only once and then used for all frequencies. It should be noted that the WFT frame formulation has been introduced originally in [8] in order to stabilize the Gabor series formulations mentioned above.

These properties were used also to extend the formulation into the TD, giving rise to the so-called PS-PBS [9], in which the field is expressed as a sum of ID-PB propagators. This method has been structured upon a new class of frames, termed the WRT frames. The use of *frames theory* provides a rigorous framework for the expansions and, at the same time, offers the wave-modeler certain degrees of freedom in choosing the most appropriate beam set for a given problem. These scalar formulations have also been extended for vector electromagnetic waves in the FD and TD [10] and [11], respectively.

A major step forward has been the proof in [12] and [13] that the beam set of the UWB-PS-BS constitutes a frame, termed "BF," not only over the aperture plane where it reduces to the standard WFT frame but also over any other plane in the propagation domain (it is interesting to note that the BF generalizes the conventional WFT and WRT frames that are structured upon Cartesian phase-space lattices, to the non-Cartesian beam-based lattices). The theory in these papers has been derived and implemented in the context of randomly rough medium scattering, and later on, in the context of local inverse scattering [14], [15]. The main goal of this paper is to demonstrate and explore the basic features of this theory within the basic context of radiation from volume source distributions. We present both UWB-FD and TD formulations. The results will be used in subsequent publications dealing with local beam-based tomographic inverse scattering [16], [17].

The presentation is divided into two parts. Sections II–IV deal with the UWB-FD formulation, while Sections V–VII deal with the TD formulation. In each part, we start with a review of the existing aperture-based formulations of [2] and [9] for the FD and TD parts, respectively (Sections II and V), then proceed with the construction of the BFs (Sections III and VI), and finally with the BF expansion of radiation from volume source distributions (Sections IV and VII). To simplify the presentation, the main text utilizes formal expressions for the frame elements, while explicit expressions for the ID frame elements are given in Appendixes A and B for the 3-D FD and TD formulations, respectively, and then in Appendix C for 2-D configurations.

II. Ultrawideband Phase-Space Beam-Summation Method (UWB-PS-BS)

We start with a brief review the UWB-PS-BS strategy [2], which provides the basis for the BF formulation presented in Section III. This theory deals with radiation from an aperture source distribution. It is based on a WFT-frame expansion of these sources, which is structured in a specific fashion so that the final field representation has the following key features.

1) The lattice of beam axes is *frequency independent*, implying that only one set of trajectories needs to be tracked in the medium, and then used for all frequencies.
2) The method utilizes the so-called ID-GBs, whose propagation in the inhomogeneous medium can be calculated analytically. Furthermore, the propagation parameters are scaled with the frequency in an "isodiffracting" fashion, implying that they are *frequency independent* [19], [20].
3) The parameter of the ID-GB is chosen such that the resulting frame expansion is *snuggest for all frequencies*, yielding a stable expansion algorithm [2], unlike the conventional Gabor expansion which is notoriously nonlocal and unstable.
4) Properties 1) and 2) above imply that the UWB-PS-BS can be effectively expressed directly in the TD using the so-called ID-PBs propagators (see Section V) [9]. These wavepackets maintain their analytic structure through propagation in inhomogeneous media, and as such may be regarded as eigenwavepacket solutions of the wave equation [19].

The theory is presented in the context of radiation into the half-space $z > 0$ with a uniform wavespeed v_0, due to a given time-harmonic field distribution $\hat{u}_0(\mathbf{x})$ over the $z = 0$ plane (Fig. 1). We use the coordinate convention $\mathbf{r} = (\mathbf{x}, z)$, $\mathbf{x} = (x_1, x_2)$, and an overcaret denotes fields with $e^{-i\omega t}$ harmonic dependence. It is assumed here that $\hat{u}_0(\mathbf{x})$ has a wide frequency band $\Omega = [\omega_{\min}, \omega_{\max}]$.

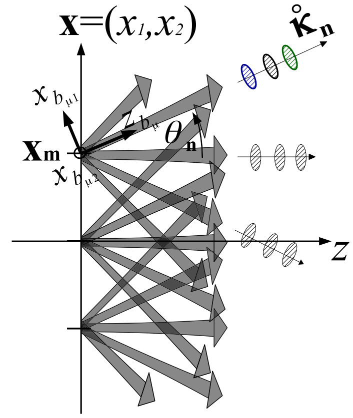

Fig. 1. BS representation of radiation from an aperture source distribution over the $z = 0$ plane. The figure depicts both the time-harmonic formulation of Section II where the propagators are beams (hatched arrows), and the TD formulation of Section V where the propagators are pulsed beam (small ellipses). The beams (or pulsed beams) emerge from the points $\mathbf{x_m}$ in the directions $\boldsymbol{\xi}_{\mathbf{n}}$. For clarity, we plot a sparse beam lattice, but actually, the lattice is denser in space, spectrum, and time such that the beams are partially overlapping. $z_{b_{\boldsymbol{\mu}}}$ and $\mathbf{x}_{b_{\boldsymbol{\mu}}}$ are the "beam coordinates" along and transverse to the $\boldsymbol{\mu}$ beam-axis, defined in (A4).

A. Windowed Fourier Transform Frame

We start by defining the plane wave spectral representation of the field

$$\hat{u}(\mathbf{r}) = \left(\frac{k}{2\pi}\right)^2 \int d^2\xi \, \hat{\tilde{u}}_0(\boldsymbol{\xi}) e^{ik(\boldsymbol{\xi}\cdot\mathbf{x}+\zeta z)}$$

with $\boldsymbol{\xi} = (\xi_1, \xi_2)$, $d^2\xi = d\xi_1 \quad d\xi_2$,

$$\zeta = \sqrt{1 - \boldsymbol{\xi}\cdot\boldsymbol{\xi}}, \quad \operatorname{Im}\zeta \geq 0, \quad k = \omega/v_0 \tag{1}$$

where $e^{ik(\boldsymbol{\xi}\cdot\mathbf{x}+\zeta z)}$ are plane-wave propagators, and the spectral function $\hat{\tilde{u}}_0(\boldsymbol{\xi})$, denoted by a tilde is defined by

$$\hat{\tilde{u}}_0(\boldsymbol{\xi}) = \int d^2x \, \hat{u}_0(\mathbf{x}) e^{-ik\boldsymbol{\xi}\cdot\mathbf{x}}. \tag{2}$$

We use the frequency-normalized spectral coordinate $\boldsymbol{\xi} = \mathbf{k}_x/k$ since it is related the plane-wave direction in a frequency independent fashion via $\boldsymbol{\xi} = (\xi_1, \xi_2) = \sin\theta(\cos\phi, \sin\phi)$. The plane waves in (1) propagate in the $\mathring{\boldsymbol{\kappa}} = (\boldsymbol{\xi}, \zeta)$ directions such that the spectral regimes $|\boldsymbol{\xi}| < 1$ and $|\boldsymbol{\xi}| > 1$ constitute, respectively, the propagation and evanescent spectra. Here and henceforth, unit vectors are denoted by an overcircle.

The PS-BS formulation is based on a WFT-frame expansion of $\hat{u}_0$. The WFT frame set over $\mathbb{L}_2(\mathbb{R}^2)$ is defined by

$$\begin{aligned}\hat{\psi}_{\boldsymbol{\mu}}(\mathbf{x}) &= \hat{\psi}(\mathbf{x} - \mathbf{x_m}) e^{ik\boldsymbol{\xi}_{\mathbf{n}}\cdot(\mathbf{x}-\mathbf{x_m})}\\ \boldsymbol{\mu} &= (\mathbf{m}, \mathbf{n}) = ((m_1, m_2), (n_1, n_2)) \in \mathbb{Z}^4\end{aligned} \tag{3}$$

where $\hat{\psi}(\mathbf{x})$ is a localized "mother window" function (typically a Gaussian). The frame elements in (3) are centered about the phase-space lattice $\mathbf{x_m} = \mathbf{m}\bar{x}$ and $\boldsymbol{\xi}_{\mathbf{n}} = \mathbf{n}\bar{\xi}$, tagged by the four-index $\boldsymbol{\mu}$ [2, Fig. 2]), with $(\bar{x}, \bar{\xi})$ being the unit cell dimensions. The set $\{\hat{\psi}_{\boldsymbol{\mu}}(\mathbf{x})\}$ in (3) constitutes a frame only if this lattice provides an overcomplete coverage of the phase space, i.e., $(\bar{x}, \bar{\xi})$ are chosen such that [2, eq. 9]

$$k\bar{\xi}\bar{x} = 2\pi\nu, \quad \nu \leq 1 \tag{4}$$

where ν is the overcompleteness parameter and $\nu \uparrow 1$ corresponds to the critically complete (or Gabor) limit.

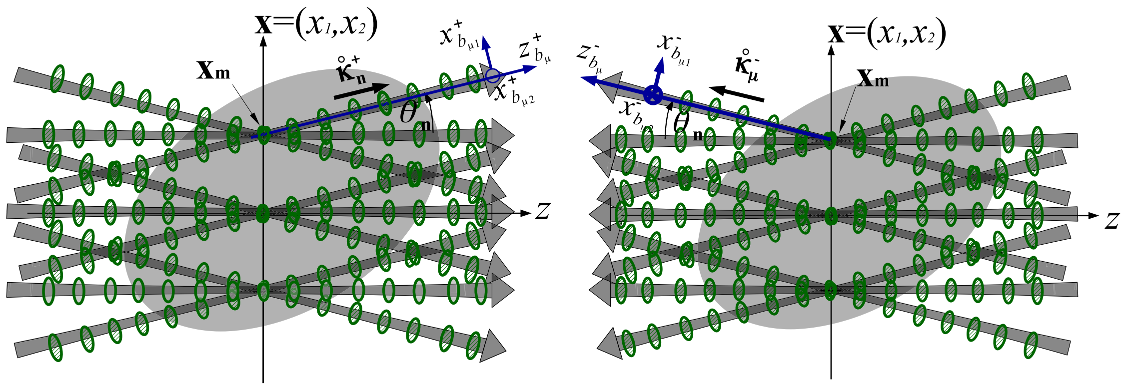

(a) $\Psi_{\boldsymbol{\mu}}^{+}$ (b) $\Psi_{\boldsymbol{\mu}}^{-}$

Fig. 2. (a) Forward and (b) backward propagating BFs $\Psi_{\boldsymbol{\mu}}^{\pm}$, respectively. The figures depict both the time-harmonic beam sets of Section III (hatched arrows) and the TD pulsed beam set of Section VI (small ellipses). The forward and backward propagating beam sets utilize the same beam skeleton with reverse beam directions. Referring to Sections IV and VII, the figures also illustrate the BF expansion for radiation from a volume source $q(\mathbf{r}, t)$.

The WFT frame can be used to expand the aperture field $\hat{u}_0(\mathbf{x})$, namely,

$$\hat{u}_0(\mathbf{x}) = \sum_{\boldsymbol{\mu}} \hat{a}_{\boldsymbol{\mu}}\, \hat{\psi}_{\boldsymbol{\mu}}(\mathbf{x}). \tag{5}$$

In view of the overcompleteness, the coefficients set $\{\hat{a}_{\boldsymbol{\mu}}\}$ is not unique. A particularly convenient set with a minimum ℓ_2-norm is obtained by using the *dual frame* $\{\hat{\varphi}_{\boldsymbol{\mu}}(\mathbf{x})\}$ which has the same structure as $\{\hat{\psi}_{\boldsymbol{\mu}}\}$ in (3) except that the "mother window" $\hat{\psi}(\mathbf{x})$ is replaced by the "dual window" $\hat{\varphi}(\mathbf{x})$. The resulting *canonical coefficient* set is given by

$$\hat{a}_{\boldsymbol{\mu}} = \langle \hat{u}_0(\mathbf{x}), \hat{\varphi}_{\boldsymbol{\mu}}(\mathbf{x})\rangle = \left(\frac{k}{2\pi}\right)^2 \langle \hat{\tilde{u}}_0(\boldsymbol{\xi}), \hat{\tilde{\varphi}}_{\boldsymbol{\mu}}(\boldsymbol{\xi})\rangle \tag{6}$$

where $\langle\, , \rangle$ denotes the conventional $\mathbb{L}_2$ inner product in the transverse coordinate $\mathbf{x}$, and the second form in (6) follows from Parseval's identity. The canonical coefficients $\hat{a}_{\boldsymbol{\mu}}$ in (6) are readily identified as the local spectrum of $\hat{u}_0(\mathbf{x})$ windowed with respect to $\hat{\varphi}_{\boldsymbol{\mu}}$ about the phase-space points $(\mathbf{x_m}, \boldsymbol{\xi}_\mathbf{n})$.

Generally, $\hat{\varphi}$ should be calculated numerically, for a given $\hat{\psi}$ and lattice $(\bar{x}, \bar{\xi})$. However, if the lattice is sufficiently overcomplete ($\nu \lesssim 1/3$), $\hat{\varphi}$ can be approximated by [2, eq. (11)]

$$\hat{\varphi}(\mathbf{x}) \approx \nu^2 \hat{\psi}(\mathbf{x})/\|\psi\|^2. \tag{7}$$

There are mainly two reasons to prefer the use of this overcomplete parameter regime, even though it implies a larger number of terms in the phase-space expansion (5): 1) as follows from (7), here $\hat{\varphi}$ is *localized* both spatially and spectrally, hence the expansion (5) comprises *local* and *stable* coefficients; 2) $\hat{\varphi}$ is given analytically in (7) and does not have to be to calculated numerically. Reason 2) is critical for UWB problems where $\hat{\varphi}$ needs to be found for each ω, and it also enables a simple transformation of $\hat{\varphi}(\mathbf{x})$ to the TD [see (B3)].

B. Beam-Summation Representation of the Radiated Field

The radiated field in $z > 0$ is obtained by substituting (5) into (1), giving

$$\hat{u}(\mathbf{r}) = \sum_{\boldsymbol{\mu}} \hat{a}_{\boldsymbol{\mu}}\, \hat{\Psi}_{\boldsymbol{\mu}}^{+}(\mathbf{r}) \tag{8}$$

$$\hat{\Psi}_{\boldsymbol{\mu}}^{+}(\mathbf{r}) = \left(\frac{k}{2\pi}\right)^2 \int d^2\xi\, \hat{\tilde{\psi}}_{\boldsymbol{\mu}}(\boldsymbol{\xi}) e^{ik(\boldsymbol{\xi}\cdot\mathbf{x}+\zeta z)}. \tag{9}$$

$\hat{\Psi}_{\boldsymbol{\mu}}^{+}(\mathbf{r})$ are the fields radiated into $z > 0$ by $\hat{\psi}_{\boldsymbol{\mu}}(\mathbf{x})$. In (9), $\hat{\tilde{\psi}}_{\boldsymbol{\mu}}(\boldsymbol{\xi}) = \hat{\tilde{\psi}}(\boldsymbol{\xi} - \boldsymbol{\xi}_\mathbf{n})e^{-ik\boldsymbol{\xi}\cdot\mathbf{x_m}}$ is the spectrum (2) of $\hat{\psi}_{\boldsymbol{\mu}}(\mathbf{x})$, with $\hat{\tilde{\psi}}(\boldsymbol{\xi})$ being the spectrum of the mother window $\hat{\psi}(\mathbf{x})$. If $\hat{\psi}(\mathbf{x})$ is wide on a wavelength scale, then $\hat{\Psi}_{\boldsymbol{\mu}}^{+}(\mathbf{r})$ behave like collimated beams, emerging from the points $\mathbf{x_m}$ in the $z = 0$ plane in the directions $\mathring{\boldsymbol{\kappa}}_\mathbf{n} = (\boldsymbol{\xi}_\mathbf{n}, \zeta_\mathbf{n}) = (\sin\theta_\mathbf{n}\cos\phi_\mathbf{n}, \sin\theta_\mathbf{n}\sin\phi_\mathbf{n}, \cos\theta_\mathbf{n})$ (see Fig. 1). However, as $\theta_\mathbf{n}$ grows, the effective width of the windows, as projected onto the beam directions, decreases and the propagators $\hat{\Psi}_{\boldsymbol{\mu}}^{+}$ become less collimated [see the collimation length $F_{\boldsymbol{\mu}1}$ in (A5)]. Indeed, it has been established in [2, Fig. 7] that the GB approximation of $\hat{\Psi}_{\boldsymbol{\mu}}^{+}$ is valid only for $\theta_\mathbf{n}$ smaller than some limiting angle that depends on the beam collimation kb. A typical value is $\theta_\mathbf{n} \lesssim 60°$, i.e., $|\boldsymbol{\xi}_\mathbf{n}| \lesssim \sqrt{3}/2$. Thus, an effective formulation using GB propagators is obtained only at observation angles smaller than 60°, or if the aperture distribution is limited to spectral values $|\boldsymbol{\xi}| \lesssim \sqrt{3}/2$. Finally, we note that for $|\boldsymbol{\xi}_\mathbf{n}| \gtrsim 1$, $\hat{\Psi}_{\boldsymbol{\mu}}^{+}$ decay exponentially with z and, therefore, can be omitted from the BS representation (8) of the radiated field.

Equation (8) expresses the radiated field as a sum of beam propagators, emerging from $\mathbf{x_m}$ on the $z = 0$ plane and propagating in the $\boldsymbol{\xi}_\mathbf{n}$ direction (Fig. 1). An important feature of this formulation is the *a priori* localization, due to the fact that the coefficients $\hat{a}_{\boldsymbol{\mu}}$ in (6) sense and emphasize the beams that match the local radiation properties of the aperture, and hence the formulation is *a priori* localized about the skeleton of geometrical optics. Further localization is due to the fact that the $\boldsymbol{\mu}$ summation in (34) accounts only for the propagators that pass near the observation point $\mathbf{r}$. The readers are referred to the discussions and examples in [2].

C. UWB Considerations

1) Frequency-Independent Beam Skeleton: We use the same $(\bar{x}, \bar{\xi})$ for all frequencies in the pertinent frequency band, thus implying that the beam lattice is frequency independent as noted in comment 1) at the beginning of Section II. It follows from (4) that

$$\nu(\omega) = \nu_{\max}\frac{\omega}{\omega_{\max}}, \quad \omega \in \Omega \tag{10}$$

where the parameter $\nu_{\max}$ is the value of ν at the highest frequency $\omega_{\max}$, so that $\nu(\omega) < \nu_{\max}$ for all $\omega \in \Omega$. As noted in connection with (7), we typically choose $\nu_{\max} \simeq 1/3$.

2) Isodiffracting Propagators: As noted in item 2) at the beginning of Section II, we use the ID-GB propagators whose favorable properties for UWB applications have been discussed there. The properties of these propagators in free space are summarized in Appendix A. They are fully determined by the frequency-independent parameter b which is actually the collimation length of the beams. Once b is chosen by the wave modeler for a given application, the lattice parameters $(\bar{x}, \bar{\xi})$ are determined via (A2) wherein we set $\nu = \nu_{\max}$ as discussed earlier. Note that if the initial conditions of the ID-GB are known, then its propagation parameters in any inhomogeneous medium can be calculated analytically.

III. Beam Frame (BF) Concept

This concept extends the WFT-frame expansion from the aperture plane to the propagation domain. It has been introduced originally in the context of propagation in fluctuating medium [12], [13]. Its application for radiation from volume source is studied in Section IV.

A. Hilbert Space of Propagating Wave Fields

The BF theory is limited to the propagating fields, hence we start by defining the Hilbert space $\mathbb{H}_P \subset \mathbb{L}_2(\mathbb{R}^2)$ of functions $\hat{u}(\mathbf{x})$, $\mathbf{x} \in \mathbb{R}^2$ with no evanescent spectrum

$$\mathbb{H}_P = \left\{\hat{u}(\mathbf{x}) \in \mathbb{L}_2(\mathbb{R}^2) \;\middle|\; \tilde{\hat{u}}(\boldsymbol{\xi}) = 0, \ \text{for } |\boldsymbol{\xi}| \geq \xi_0\right\} \tag{11}$$

with $\xi_0 < 1$ is a parameter that depends on the properties of the sources. Following the discussion after (9), we typically consider fields with limited spectral spread $\theta_0 \lesssim 60°$, hence $\xi_0 = \sin\theta_0 \lesssim \sqrt{3}/2$.

Recalling from (3) that $\hat{\psi}_{\boldsymbol{\mu}}$ are centered around $\boldsymbol{\xi}_{\mathbf{n}}$, it follows that $\hat{u} \in \mathbb{H}_P$ can be expanded using a subset of the frameset $\{\hat{\psi}_{\boldsymbol{\mu}}(\mathbf{x})\}$ in (3), tagged by the index set $\boldsymbol{\mu}_P = \left\{\boldsymbol{\mu} = (\mathbf{m};\, \mathbf{n}) \in \mathbb{Z}^4 \;\middle|\; |\mathbf{n}| < (\xi_0/\bar{\xi}) + n_0\right\}$, where n_0 is a parameter that accounts for elements whose centers $\boldsymbol{\xi}_{\mathbf{n}}$ lie just outside the circle $|\boldsymbol{\xi}| < \xi_0$ which may contain some spectral contributions inside that circle (typically $n_0 \sim 1$).

B. Forward and Backward Propagating Beam Frames

We start by noting that spectral integral (9) defines the forward propagating beams not only for $z > 0$ but also for $z < 0$. Thus, the beam set $\{\hat{\Psi}^+_{\boldsymbol{\mu}}(\mathbf{r})\}_{\boldsymbol{\mu}_P}$ is forward propagating from $z = -\infty$ to ∞, converging at $z = 0$ to the WFT frame set $\hat{\psi}_{\boldsymbol{\mu}}(\mathbf{x})$ of (3), as depicted in Fig. 2(a).

Likewise replacing $\zeta \to -\zeta$ in the spectral integral (9) defines the beam-set $\{\hat{\Psi}^-_{\boldsymbol{\mu}}(\mathbf{r})\}_{\boldsymbol{\mu}_P}$ that are backward propagating from $z = \infty$ to $-\infty$, converging at $z = 0$ to the same WFT frame set $\hat{\psi}_{\boldsymbol{\mu}}(\mathbf{x})$, as depicted in Fig. 2(b).

We also define the sets of forward and backward beam waves $\hat{\Phi}^{\pm}_{\boldsymbol{\mu}}(\mathbf{r})$, given by (9) but with $\tilde{\hat{\psi}}_{\boldsymbol{\mu}}(\boldsymbol{\xi})$ replaced by $\tilde{\hat{\varphi}}_{\boldsymbol{\mu}}(\boldsymbol{\xi})$. Clearly, the properties of the sets $\hat{\Phi}^{\pm}_{\boldsymbol{\mu}}(\mathbf{r})$ are similar to those of $\hat{\Psi}^{\pm}_{\boldsymbol{\mu}}(\mathbf{r})$ as discussed earlier. In particular, at the $z = 0$ plane, they reduce to the dual-WFT frame set $\hat{\varphi}_{\boldsymbol{\mu}}(\mathbf{x})$. Note also from (7) that in the highly overcomplete parameter regime used, $\hat{\Phi}^{\pm}_{\boldsymbol{\mu}}$ are proportional to $\hat{\Psi}^{\pm}_{\boldsymbol{\mu}}$.

C. Beam-Frame Theorems

The BF theory is based on the following theorems that have been proved in [12, Appendix A].

Theorem 1 (Beam-Frame Theorem): The forward/backward propagating beam sets $\{\hat{\Psi}^{\pm}_{\boldsymbol{\mu}}(\mathbf{r})\}$ constitute frames over $\mathbb{H}_P$ at any given plane $z = const$, with $\{\hat{\Phi}^{\pm}_{\boldsymbol{\mu}}(\mathbf{r})\}$ being their canonical dual frames.

The theorem implies that any function $\hat{f}(\mathbf{x}) \in \mathbb{H}_P$ defined over a given $z = const.$ plane can be expanded using either the $\hat{\Psi}^+_{\boldsymbol{\mu}}$ or the $\hat{\Psi}^-_{\boldsymbol{\mu}}$ sets on that plane. A special case of interest is when the function to be expanded is a forward propagating wavefield $\hat{u}^+(\mathbf{r})$. In view of Theorem 1, it can be expanded over any $z = const$ plane using either the $\hat{\Psi}^+_{\boldsymbol{\mu}}$ set or the $\hat{\Psi}^-_{\boldsymbol{\mu}}$ set at that plane. However, since $\hat{u}^+$ is forward propagating, it makes sense to expand it using the forward propagating set $\hat{\Psi}^+_{\boldsymbol{\mu}}$, namely,

$$\hat{u}^+(\mathbf{r}) = \sum_{\boldsymbol{\mu} \in \boldsymbol{\mu}_P} \hat{A}^+_{\boldsymbol{\mu}}(z)\hat{\Psi}^+_{\boldsymbol{\mu}}(\mathbf{r}), \quad \hat{A}^+_{\boldsymbol{\mu}}(z) = \left\langle \hat{u}^+(\mathbf{r}), \hat{\Phi}^+_{\boldsymbol{\mu}}(\mathbf{r}) \right\rangle\Big|_z.$$

Note that by definition, for any given $\mathbf{r}$, the expansion coefficients $\hat{A}^+_{\boldsymbol{\mu}}$ are calculated over the corresponding z plane. For propagating wavefields, however, this restriction can be removed as summarized in the following theorem [12, Appendix B]:

Theorem 2 (The Coefficient Invariance Theorem): Let $\hat{u}^{\pm}(\mathbf{r})$ be forward/backward propagating wavefields in a uniform medium, with no evanescent spectra. They may be expanded using the forward/backward propagating BFs, respectively, such that the coefficient sets $\{\hat{A}^{\pm}_{\boldsymbol{\mu}}\}$ are independent of z.

In view of this theorem, any forward/backward propagating wavefields $\hat{u}^{\pm}$ can be expanded as

$$\hat{u}^{\pm}(\mathbf{r}) = \sum_{\boldsymbol{\mu} \in \boldsymbol{\mu}_P} \hat{A}^{\pm}_{\boldsymbol{\mu}}\hat{\Psi}^{\pm}_{\boldsymbol{\mu}}(\mathbf{r}) \tag{12}$$

where the expansion coefficients are given as

$$\hat{A}^{\pm}_{\boldsymbol{\mu}} = \left\langle \hat{u}^{\pm}(\mathbf{r}'), \hat{\Phi}^{\pm}_{\boldsymbol{\mu}}(\mathbf{r}') \right\rangle\Big|_{z'} \tag{13a}$$

$$= \left\langle \hat{u}^{\pm}_0(\mathbf{x}'), \hat{\varphi}_{\boldsymbol{\mu}}(\mathbf{x}') \right\rangle\Big|_{z'=0} = \hat{a}^{\pm}_{\boldsymbol{\mu}} \tag{13b}$$

where z' in (13a) is arbitrary, while in (13b), we calculate the coefficients on the $z' = 0$ plane as in (6).

IV. Beam-Frame Representation of Radiation From a Volume Sources

The BF formulation generalizes the conventional plane-wave spectrum representation in wave theory as it can be used for local expansion of the sources (real or induced) and of the resulting fields. As an example, we apply it here for the basic problem of radiation from a volume source distribution $\hat{q}$, described by the wave equation

$$[\nabla^2 + k^2]\hat{u}(\mathbf{r}) = -\hat{q}(\mathbf{r}), \quad \hat{q} \text{ bounded between } z^{\pm}. \tag{14}$$

The solution to (14) can be expressed as

$$\hat{u}(\mathbf{r}) = \int d^3r'\, \hat{q}(\mathbf{r}')\hat{G}(\mathbf{r}, \mathbf{r}') \tag{15}$$

where $\hat{G}(\mathbf{r},\mathbf{r}') = e^{ik|\mathbf{r}-\mathbf{r}'|}/4\pi|\mathbf{r}-\mathbf{r}'|$ is the free-space Green's function.

The BF expansion of the field has the form (12), namely,

$$\hat{u}^{\pm}(\mathbf{r}) = \sum_{\boldsymbol{\mu}} \hat{A}^{\pm}_{\boldsymbol{\mu}} \hat{\Psi}^{\pm}_{\boldsymbol{\mu}}(\mathbf{r}), \quad \text{for } z \gtrless z^{\pm}. \tag{16}$$

Next, we express $\hat{A}^{\pm}$ as a BF expansion of $\hat{q}(\mathbf{r})$. Referring to the coefficient invariance Theorem 2, $\hat{A}^{\pm}$ can be calculated on any z' plane such that $z' \gtrless z^{\pm}$, respectively. Therefore, we calculate $\hat{A}^{\pm}$ on the planes $z^{\pm}$ via (13a), obtaining (cf. [12, eqs. (35) and (36)])

$$\hat{A}^{\pm}_{\boldsymbol{\mu}} = \left(\frac{k}{2\pi}\right)^2 \langle \hat{\tilde{u}}(\boldsymbol{\xi}, z), \hat{\tilde{\Phi}}^{\pm}_{\boldsymbol{\mu}}(\boldsymbol{\xi}, z)\rangle\big|_{z^{\pm}} \tag{17a}$$

$$= \left(\frac{k}{2\pi}\right)^2 \int d^2\xi \int_{z^-}^{z^+} dz'' \hat{\tilde{q}}(\boldsymbol{\xi}, z'') \frac{e^{ik\zeta|z^{\pm}-z''|}}{-2ik\zeta} \times [\hat{\tilde{\varphi}}_{\boldsymbol{\mu}}(\boldsymbol{\xi}) e^{\pm ik\zeta z^{\pm}}]^* \tag{17b}$$

$$= \int_{z^-}^{z^+} dz'' \left(\frac{k}{2\pi}\right)^2 \int d^2\xi\, \hat{\tilde{q}}(\boldsymbol{\xi}, z'') \left[\frac{\hat{\tilde{\varphi}}_{\boldsymbol{\mu}}(\boldsymbol{\xi}) e^{\pm ik\zeta z''}}{2ik\zeta}\right]^* \tag{17c}$$

$$= \int_{z^-}^{z^+} dz'' \left(\frac{k}{2\pi}\right)^2 \int d^2\xi\, \hat{\tilde{q}}(\boldsymbol{\xi}, z'') \big[\hat{\tilde{\Phi}}^{G\pm}_{\boldsymbol{\mu}}(\boldsymbol{\xi}, z'')\big]^* \tag{17d}$$

$$= \int_{z^-}^{z^+} dz'' \langle \hat{q}(\mathbf{r}''), \hat{\Phi}^{G\pm}_{\boldsymbol{\mu}}(\mathbf{r}'')\rangle. \tag{17e}$$

Equation (17a) is the spectral (Parseval) counterpart of (13a) evaluated over the $z' = z^{\pm}$ plane. In the first line in (17b), we used the spectral form of Green's function solution (15), and in the second line, we used the spectral definition of $\hat{\Phi}^{\pm}_{\boldsymbol{\mu}}$, namely, $\hat{\tilde{\Phi}}^{\pm}_{\boldsymbol{\mu}} = \hat{\tilde{\varphi}}_{\boldsymbol{\mu}}(\boldsymbol{\xi}) e^{\pm ik\zeta z}$, as follows from (9) and the discussion in Section III-B. Then, (17d) defines the propagators $\hat{\tilde{\Phi}}^{G\pm}_{\boldsymbol{\mu}}(\boldsymbol{\xi}, z'')$, and finally (17e) is the spatial counterpart of (17d). The final result in (17e) can be expressed as

$$\hat{A}^{\pm}_{\boldsymbol{\mu}} = \int_V d^3r\, \hat{q}(\mathbf{r}) \big[\hat{\Phi}^{G\pm}_{\boldsymbol{\mu}}(\mathbf{r})\big]^* \stackrel{\text{def}}{=} \langle \hat{q}(\mathbf{r}), \hat{\Phi}^{G\pm}_{\boldsymbol{\mu}}(\mathbf{r})\rangle_V \tag{18}$$

where from (17d), $\hat{\Phi}^{G\pm}_{\boldsymbol{\mu}}(\mathbf{r})$ are the beam-based Green's functions

$$\hat{\Phi}^{G\pm}_{\boldsymbol{\mu}}(\mathbf{r}) = \left(\frac{k}{2\pi}\right)^2 \int d^2\xi\, e^{ik(\boldsymbol{\xi}\cdot\mathbf{x} \pm \zeta z)} \frac{1}{2ik\zeta} \hat{\tilde{\varphi}}_{\boldsymbol{\mu}}(\boldsymbol{\xi}) \tag{19a}$$

$$\simeq \frac{1}{2ik\cos\theta_{\mathbf{n}}} \hat{\Phi}^{\pm}_{\boldsymbol{\mu}}(\mathbf{r}). \tag{19b}$$

The approximation in (19b) applies for the high-collimation case where $\hat{\tilde{\varphi}}_{\boldsymbol{\mu}}$ is localized about the spectral direction $\boldsymbol{\xi}_{\mathbf{n}}$ [see discussion after (9)] so that we may replace $\zeta \approx \zeta_{\mathbf{n}} = \cos\theta_{\mathbf{n}}$ in the amplitude. The spectral integral is then recognized as $\hat{\Phi}^{\pm}_{\boldsymbol{\mu}}$ [see (9) and the discussion in Section III-B]. Note that in view of (7), $\hat{\Phi}^{G\pm}_{\boldsymbol{\mu}}(\mathbf{r})$ is proportional to $\hat{\Psi}^{\pm}_{\boldsymbol{\mu}}(\mathbf{r})$.

Equation (18) is the main result in this section. It expresses $\hat{A}^{\pm}_{\boldsymbol{\mu}}$ as a projection of $\hat{q}(\mathbf{r})$ onto the forward/backward propagating beams $\hat{\Phi}^{\pm}_{\boldsymbol{\mu}}(\mathbf{r})$ (see Fig. 2). This formulation generalizes the K-space formulation, where the field is expressed as a superposition of plane waves whose amplitude (the K-domain spectrum) is obtained by projecting $\hat{q}$ onto the plane-wave propagators $\hat{\Psi}^{\pm}_{\xi}(\mathbf{r}) = e^{ik\mathring{\boldsymbol{\kappa}}\cdot\mathbf{r}}$, $\mathring{\boldsymbol{\kappa}} = (\boldsymbol{\xi}, \pm\zeta)$. Thus, the BF beam formulation in (16)–(18) is a step between Green's function formulation (15), where $\hat{q}$ is described as a sum of point sources, and the K-space formulation where $\hat{q}$ is described as plane-wave sources.

A. Example A: A Source With an Axial Phase Progression

For simplicity, we consider a 2-D problem, $\boldsymbol{\rho} = (x, z)$, with time-harmonic source distribution

$$\hat{q}(\boldsymbol{\rho}) = \hat{q}_0\, e^{i\omega z/v_q} \quad \text{for } |\boldsymbol{\rho}| < a \text{ and } 0 \text{ otherwise} \tag{20}$$

where $\hat{q}_0$ is a constant, and v_q defines the speed of the phase progression of along the z-axis. We choose $v_q = 0.8v_0$ where the units are normalized such that $v_0 = 1$. The frequency band is $\omega = [\omega_{\min}, \omega_{\max}]$ with $\omega_{\max} = 1$ and $\omega_{\min} = 0.5\omega_{\max}$, such that the free-space wavelength is $\lambda|_{\omega_{\max}} = 2\pi$. The source support is taken to be $a = 20\pi$ and is large on a wavelength scale at all pertinent frequencies. The reference solution is calculated via Green's function integration (15) using the 2-D Green's function $\hat{G}(\boldsymbol{\rho}, \boldsymbol{\rho}') = (-i/4)H_0^{(1)}(k|\boldsymbol{\rho} - \boldsymbol{\rho}'|)$.

1) Choosing the Expansion Parameters: We use ID-GB beam set in Appendix C-A. We choose the collimation $b = 100$ to be larger than a, and $\nu_{\max} = 0.3$ as discussed in (10). Given b and $\nu_{\max}$, the phase-space unit cell is calculated via (A2), giving $(\bar{x}, \bar{\xi}) = (13.73, 0.1373)$. The spatial resolution is determined by the beamwidth W_0 of (A6), and it varies between ~ 10 and $\sim 10\sqrt{2}$ for $\omega_{\max}$ and $\omega_{\min}$, respectively.

2) Expansion Coefficients: The expansion coefficients $\hat{A}^{\pm}_{\boldsymbol{\mu}}$ are calculated via (18) with the beam kernels $\hat{\Phi}^{G\pm}_{\boldsymbol{\mu}}$ given in (C3). We consider only those beams that pass no more than three beamwidths away from the support of $\hat{q}$, where the beamwidth $W_{\boldsymbol{\mu}\ell}(z_b)$ is given by the $\ell = 1$ term in (A6).

Henceforth, we shall be interested only in the field for $z > 0$, described by the forward propagating BF $\hat{\Psi}^{+}_{\boldsymbol{\mu}}$. The magnitude of $\hat{A}^{+}_{\boldsymbol{\mu}}$ is plotted in Fig. 3, for $\omega = 0.7$ and 1. One discerns that, as expected, the beams that match the *local phase-space distribution* of the source are strongly excited. Spatially, this implies that these beam pass through the support of $\hat{q}(\boldsymbol{\rho})$, while spectrally, they should match the local phase distribution of $\hat{q}(\boldsymbol{\rho})$. Noting that the phase progression of the source is $\exp(i\omega z/v_q)$, while the phase progression of the propagators is controlled by $\exp(i\omega z_{b_{\boldsymbol{\mu}}}/v_0)$ where $z_{b_{\boldsymbol{\mu}}}$, the coordinate along the beam axis, is given by $z_{b_{\boldsymbol{\mu}}} = z/\zeta_n$ with $\zeta_n = \cos\theta_n = \sqrt{1 - \xi_n^2}$, it follows that the coefficients are localized in the phase-space zone $\zeta_n \approx v_q/v_0$.

We also observe that the coefficients $\hat{A}^{+}_{\boldsymbol{\mu}}$ near $(m, n) = (0, 0)$ vanish for $\omega = 1$ but not for $\omega = 0.7$. We would like to clarify that these coefficients are oscillatory functions of ω due to the ratio between $\lambda(\omega)$, a, and v_q, so that vanishing at $\omega = 1$ is only a coincidence.

Finally, one discerns that the beams that pass near the boundaries of $\hat{q}$ sense the sharp truncation of $\hat{q}$ at $|\boldsymbol{\rho}| = a$ and are strongly excited. They can be deemphasized when the truncation of $\hat{q}$ in (20) is smoother. This diffraction effect is related to the *diffraction manifolds* identified in [1], [2], and [4].

3) BS Calculation of the Field: The radiated field calculated via the BS (16) is depicted in Fig. 4 for observation points at the $z = 100$ plane. We threshold out the weakly excited beams at a level of 1% and out of those we sum only

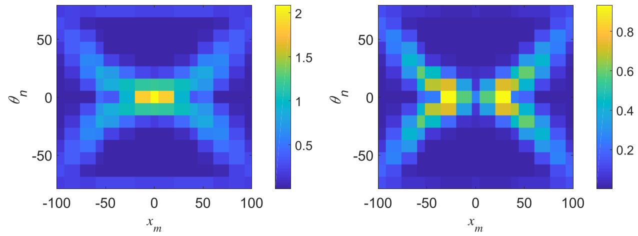

(a) (b)

Fig. 3. Magnitude of the expansion coefficients $\hat{A}^{+}_{\boldsymbol{\mu}}$ in the (x_m, θ_n) phase space for (a) $\omega = 0.7$ and (b) $\omega = 1$. Note the scale difference of the color bars.

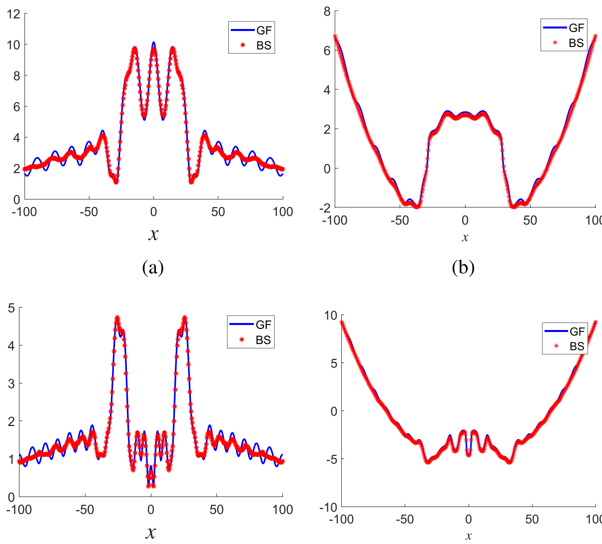

(a) (b)

(c) (d)

Fig. 4. Radiated field at $z = 100$. The figure compares the BS results (red points) to Green's function integration in (15) (solid blue lines). (a) and (b) $\omega = 0.7$. (c) and (d) $\omega = 1$.

those that pass within a three-beamwidth neighborhood of the observation point. *This renders the field described by relatively few elements which, nevertheless, capture the main physics* (see Fig. 3). Indeed, the results are in an excellent agreement with the reference solution, with a small deterioration in the accuracy at large angles which is an inherent property of the BS approach as discussed after (9). We also note that the phase remains more accurate, as needed for recovering of the TD field.

B. Example B: A Source With an Oblique Forward/Backward Phase Progression

Here, the source distribution has the form [see (20)]

$$\hat{q}(\boldsymbol{\rho}) = \hat{q}_0 e^{i\omega\mathring{\boldsymbol{\kappa}}_q\cdot\boldsymbol{\rho}/v_q} + \hat{q}_0 e^{-i\omega\mathring{\boldsymbol{\kappa}}_q\cdot\boldsymbol{\rho}/v_q}, \quad |\boldsymbol{\rho}| < a \tag{21}$$

where $\mathring{\boldsymbol{\kappa}}_q = (\sin\theta_q, \cos\theta_q)$ and v_q are the direction and speed of the phase progression in $\hat{q}(\boldsymbol{\rho})$. The first and second terms in (21) represent sources with phase progression in the positive and negative $\mathring{\boldsymbol{\kappa}}_q$ directions, henceforth referred to as $\hat{q}^{\pm}$, respectively. In the following, we choose $\theta_q = 30^\circ$ and $v_q = 0.8v_0$ and calculate the radiated filed at $z = 100$. It is expected that the dominant contribution there will be due to $\hat{q}^{+}$.

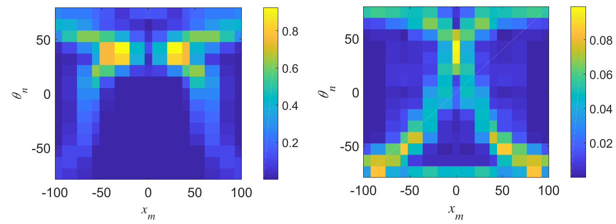

(a) (b)

Fig. 5. Expansion coefficients $\hat{A}^{+}_{\boldsymbol{\mu}}$ in the (x_m, θ_n) phase space due to (a) $\hat{q}^{+}$ and (b) $\hat{q}^{-}$ in (21). Here, $\omega = 1$. Note the scale difference between the figures.

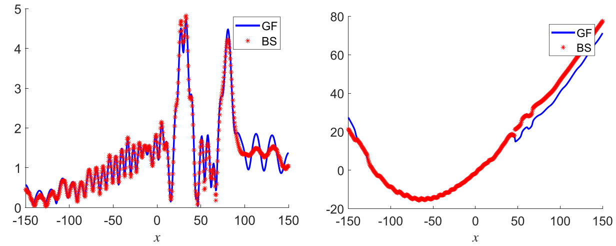

(a) (b)

Fig. 6. Radiated field at $z = 100$ for $\omega = 1$. The figure compares the BS results (red points) to Green's function integration in (15) (solid blue lines).

1) Expansion Coefficients: The field at $z = 100$ is expressed in terms of the beam set $\hat{\Psi}^{+}_{\boldsymbol{\mu}}$ as in (16). We use the same expansion parameters as in the example of Section IV-A1. The respective amplitudes $\hat{A}^{+}_{\boldsymbol{\mu}}$ are plotted in Fig. 5 where we show separately the contribution due to $\hat{q}^{+}$ and $\hat{q}^{-}$. As expected, those due to $\hat{q}^{-}$ are negligible, so that $\hat{A}^{+}_{\boldsymbol{\mu}}$ are dominated by the contribution of $\hat{q}^{+}$ in Fig. 5(a). Noting that the phase progression of $\hat{q}^{+}$ along the $\mathring{\boldsymbol{\kappa}}_q$-axis is $\exp(i\omega z/v_q \cos\theta_q)$, while the phase progression of $\hat{\Psi}^{+}_{\boldsymbol{\mu}}$ along their axes is given by $\exp(i\omega z_{b_{\boldsymbol{\mu}}}/v_0)$ where $z_{b_{\boldsymbol{\mu}}}$, the coordinates along the beam axes, is given by $z_{b_{\boldsymbol{\mu}}} = z/\cos\theta_n$, it follows that the coefficients are localized in the phase-space range $\cos\theta_n \approx (v_q/v_0)\cos\theta_q$, giving in our case $n = 5$ as readily seen in Fig. 5(a). As in the example of Section IV-A, one also discerns diffraction effects due to beam that pass near the edges of $\hat{q}$.

2) BS Calculation of the Field: Finally, the radiated field is calculated as in Section IV-A3 where, as discussed there, we only keep the beams whose amplitudes $\hat{A}^{+}_{\boldsymbol{\mu}}$ are at least 1% of the largest amplitude, and out of these, we sum only those passing within a three-beamwidth neighborhood of the observation point. Nevertheless, one observes that the BS result in Fig. 6 captures the main physics and is in a good agreement with the exact Green's function result, with a small deterioration at large angles, as discussed after (9).

V. Phase-Space Pulsed-Beam Summation (PS-PBS)

As noted in the Introduction, the UWB-PS-BS can be expressed directly in the TD. In this section, we summarize the WRT-frame theory of [9] which addresses radiation due to an aperture source distribution $u_0(\mathbf{x}, t)$ over the $z = 0$. In Sections VI and VII, the theory will be generalized in terms of the PB frame (PBF) and then applied for radiation from a time-dependent volume source distribution $q(\mathbf{r}, t)$.

Following Section II, it is assumed that $u_0 \in \mathbb{L}_2^{\Omega}(\mathbb{R}^2 \times \mathbb{R})$, the Hilbert space of square integrable distributions in $(\mathbf{x}, t)$

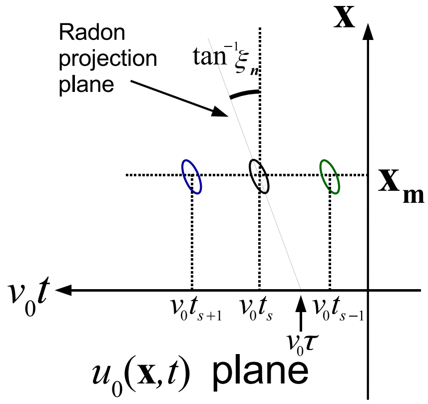

Fig. 7. Slant stack transform (slanted lines) and the windowed-SST or WRT (small ellipses) in the 3-D $(\mathbf{x}, t)$ domain. The slant is defined via $(v_0\ dt/d\mathbf{x}) = \boldsymbol{\xi}_\mathbf{n}$.

whose frequency spectrum is within $\Omega = [\omega_{\min}, \omega_{\max}]$. Henceforth, time and FD constituents are related via the Fourier transform

$$\hat{u}(\omega) = \int_{-\infty}^{\infty} dt\, e^{i\omega t} u(t). \tag{22}$$

A. Time-Dependent Plane-Wave Formulation

We start by defining the "conventional" time-dependent plane-wave spectrum $\tilde{u}_0(\boldsymbol{\xi}, \tau)$ of $u_0(\mathbf{x}, t)$, which is the TD counterpart of $\hat{\tilde{u}}_0(\boldsymbol{\xi}, \omega)$ of (2). Applying the inverse Fourier transform to (2) and evaluating the ω-integration in a closed form yields the TD plane-wave transform [9], [22]

$$\tilde{u}_0(\boldsymbol{\xi}, \tau) = \int d^2x\, u_0\big(\mathbf{x}, \tau + v_0^{-1}\boldsymbol{\xi}\cdot\mathbf{x}\big). \tag{23}$$

Equation (23) is also referred to as a slant-stack transform (SST) since it consists of projections of $u_0(\mathbf{x}, t)$ along the slanted delay surfaces $t - v_0^{-1}\boldsymbol{\xi}\cdot\mathbf{x} = \tau = const$ in the 3-D $(\mathbf{x}, v_0\, t)$ data domain (see Fig. 7). Consequently, it extracts from $u_0(\mathbf{x}, t)$ the waveform of the time-dependent plane waves $\tilde{u}_0(\boldsymbol{\xi}, \tau)$ that propagate in the direction $\mathring{\boldsymbol{\kappa}} = (\boldsymbol{\xi}, \zeta)$ of (1). For $|\boldsymbol{\xi}| < 1$, the slant angle is smaller than $\pi/4$ and the resulting plane wave is "propagating," whereas for $|\boldsymbol{\xi}| > 1$, the slant is larger and the plane waves are "evanescent," i.e., decay away from the $z = 0$ plane.

The radiated field for $z > 0$ is obtained by propagating the pulsed plane-wave spectrum in (23). The expression is obtained by inverting (1) into the TD. This procedure, however, requires an analytic signal formulation since ζ is complex for $|\boldsymbol{\xi}| > 1$, thus leading to a complex propagation delay [1], [22]. The analytic signal corresponding to the frequency spectrum $\hat{u}(\omega)$ is defined via the one-side inverse Fourier transform of (22), namely,

$$\overset{+}{u}(t) = \frac{1}{\pi}\int_0^{\infty} d\omega\, e^{-i\omega t}\hat{u}(\omega), \quad \operatorname{Im} t \le 0. \tag{24}$$

Clearly, the integral in (24) defines an analytic function in the lower half of the complex t plane, whose limit on the real t axis defines the real (physical) signal $u(t)$ via

$$\overset{+}{u}(t) = u(t) + i\mathcal{H}\{u(t)\}, \quad t \text{ real}. \tag{25}$$

where $\mathcal{H}$ denotes the Hilbert transform. It follows that the *physical* field for real t is given by $u(t) = \operatorname{Re}\overset{+}{u}(t)$. Henceforth, analytic signals are denoted by an overplus.

By applying now (24) to (1) and evaluating the ω integration in a closed form, we obtain

$$\overset{+}{u}(\mathbf{r}, t) = \frac{-1}{(2\pi v_0)^2}\int d^2\xi\, \partial_t^2 \overset{+}{\tilde{u}}_0[\boldsymbol{\xi}, t - v_0^{-1}(\boldsymbol{\xi}\cdot\mathbf{x} + \zeta z)]. \tag{26}$$

In many cases, including the present, one is interested only with the contributions of the propagating spectrum $|\boldsymbol{\xi}| < 1$. Here, ζ is real, hence (26) reduces to the real signal expression

$$u_{\text{prop}}(\mathbf{r}, t) = \frac{-1}{(2\pi v_0)^2}\int_{|\boldsymbol{\xi}|<1} d^2\xi\, \partial_t^2 \tilde{u}_0\big[\boldsymbol{\xi}, t - v_0^{-1}(\boldsymbol{\xi}\cdot\mathbf{x} + \zeta z)\big]. \tag{27}$$

B. Windowed Radon Transform (WRT) Frames

Referring to Section II, let $\hat{\psi}(\mathbf{x}, \omega)$ and $\hat{\varphi}(\mathbf{x}, \omega)$ be the dual window functions corresponding to the WFT-frame over the phase-space lattice $(\bar{x}, \bar{\xi})$ for all $\omega \in \boldsymbol{\Omega}$. Outside $\boldsymbol{\Omega}$, these functions can be chosen quite arbitrarily, hence we choose them such that they taper smoothly to zero, thus yielding smooth and localized spatiotemporal windows (see B1). Inverting these functions to the TD defines the space-time "mother" windows $\psi(\mathbf{x}, t)$ and $\varphi(\mathbf{x}, t)$. Note in (7) that in the highly overcomplete regime which is used here, φ can be evaluated from ψ (see the ID windows in (B3)).

The WRT frames are structured upon a discrete 5-D lattice in the $(\mathbf{x}, t)$ domain [cf. (3)]

$$(\mathbf{x}_\mathbf{m}, \boldsymbol{\xi}_\mathbf{n}, t_s) = (\mathbf{m}\bar{x}, \mathbf{n}\bar{\xi}, s\bar{t}), \ (\mathbf{m}, \mathbf{n}, s) \overset{\text{def}}{=} (\boldsymbol{\mu}, s) \in \mathbb{Z}^5. \tag{28}$$

The temporal sampling rate $\bar{t}$ satisfies

$$\bar{t} \le \frac{2\pi}{\omega_{\max} + \omega_h} \tag{29}$$

where ω_h, the highest frequency in $\hat{\psi}$ and $\hat{\varphi}$, is taken to be outside $\boldsymbol{\Omega}$ (i.e., $\omega_h \ge \omega_{\max}$). The choice of ω_h poses a tradeoff between having more localized space-time propagators for larger ω_h while at the same time keeping $\bar{t}$ sufficiently large to reduce the number of elements in the field representation.

The WRT frames sets $\{\psi_{\boldsymbol{\mu},s}\}$ and $\{\varphi_{\boldsymbol{\mu},s}\}$ are now obtained by inverting $\hat{\psi}_{\boldsymbol{\mu}}$, $\hat{\varphi}_{\boldsymbol{\mu}}$ into the time coordinate $t - t_s$, giving [9, eq. (14)]

$$\psi_{\boldsymbol{\mu},s}(\mathbf{x}, t) = \psi[\mathbf{x} - \mathbf{x}_\mathbf{m},\ t - t_s - v_0^{-1}\boldsymbol{\xi}_\mathbf{n}\cdot(\mathbf{x} - \mathbf{x}_\mathbf{m})] \tag{30}$$

$$\varphi_{\boldsymbol{\mu},s}(\mathbf{x}, t) = \bar{t}\,\varphi[\mathbf{x} - \mathbf{x}_\mathbf{m},\ t - t_s - v_0^{-1}\boldsymbol{\xi}_n\cdot(\mathbf{x} - \mathbf{x}_\mathbf{m})]. \tag{31}$$

Note that $\varphi_{\boldsymbol{\mu},s}$ is multiplied by the sampling scale $\bar{t}$. As schematized in Fig. 7, the frame elements $\psi_{\boldsymbol{\mu},s}$ and $\varphi_{\boldsymbol{\mu},s}$ are centered about the point $(\mathbf{x}_\mathbf{m}, t_s)$ in the $(\mathbf{x}, t)$ plane, with a spectral slant $\boldsymbol{\xi}_n$, hence the WRT designation. A proof that these sets constitute dual-frame set is given in [9, Appendix B].

The WRT frame expansion of the field $u_0(\mathbf{x}, t)$ over the $z = 0$ plane is obtain now by inverting (5) and (6) into the TD, also using the sampling theorem for functions in Ω, obtaining [9, eq. (15)]

$$u_0(\mathbf{x},t) = \sum_{\boldsymbol{\mu},s} a_{\boldsymbol{\mu},s}\,\psi_{\boldsymbol{\mu},s}(\mathbf{x},t) \tag{32}$$

$$\begin{aligned} a_{\boldsymbol{\mu},s} &= \int d^2x \int dt\, u_0(\mathbf{x},t)\varphi_{\boldsymbol{\mu},s}(\mathbf{x},t) \\ &= \langle u_0(\mathbf{x},t), \varphi_{\boldsymbol{\mu},s}(\mathbf{x},t)\rangle. \end{aligned} \tag{33}$$

Note that $a_{\boldsymbol{\mu},s} = \bar{t} a_{\boldsymbol{\mu}}(t_s)$, where $a_{\boldsymbol{\mu}}(t)$ is the TD counterpart of $\hat{a}_{\boldsymbol{\mu}}(\omega)$ of (6).

Equation (33) expresses $a_{\boldsymbol{\mu},s}$ as a projection of the data $u_0(\mathbf{x},t)$ onto the window $\varphi_{\boldsymbol{\mu},s}(\mathbf{x},t)$. By comparing this projection to the SST in (23) as illustrated in Fig. 7, it is identified as a local-SST of u_0 about $(\mathbf{x},t) = (\mathbf{x_m}, t_s)$ with spectral tilt $\boldsymbol{\xi}_\mathbf{n}$. The inverse transform (32) then reconstructs $u_0(\mathbf{x},t)$ as a sum of the shifted and tilted window functions $\psi_{\boldsymbol{\mu},s}(\mathbf{x},t)$.

C. PS-PBS Representation of the Radiated Field

The expansion of the aperture source $u_0(\mathbf{x},t)$ in (32) can be propagated into the $z > 0$ domain, giving

$$u(\mathbf{r},t) = \sum_{\boldsymbol{\mu},s} a_{\boldsymbol{\mu},s}\Psi^+_{\boldsymbol{\mu},s}(\mathbf{r},t) \tag{34}$$

where $\Psi^+_{\boldsymbol{\mu},s}(\mathbf{r},t)$ are the propagating fields due to the window functions $\psi_{\boldsymbol{\mu},s}(\mathbf{x},t)$ in the $z = 0$ plane. Since $\psi_{\boldsymbol{\mu},s}$ are centered about the points $(\mathbf{x_m}, t_s)$ in the $(\mathbf{x},t)$ plane, with a spectral slant $\boldsymbol{\xi}_n$ (see Fig. 7), it follows that $\Psi^+_{\boldsymbol{\mu},s}$ are PB fields that emerge from the points $\mathbf{x_m}$ over the $z = 0$ plane, at times t_s and propagate in the $\mathring{\boldsymbol{\kappa}}_\mathbf{n}$ directions defined after (9). Propagating PB occur only for $|\boldsymbol{\xi}_\mathbf{n}| \lesssim 1$, whereas for $|\boldsymbol{\xi}_\mathbf{n}| \gtrsim 1$, $\Psi^+_{\boldsymbol{\mu},s}$ decay with z and can be omitted from the BS (34) for the radiated field. For radiation problems, we need only the propagating PBs with $\boldsymbol{\xi}_\mathbf{n}$ in the propagating spectrum, which are given by [cf. (27)]

$$\Psi^+_{\boldsymbol{\mu},s}(\mathbf{r},t) = \frac{-1}{(2\pi v_0)^2}\int_{|\boldsymbol{\xi}|<1} d^2\xi\, \partial_t^2 \tilde{\psi}_{\boldsymbol{\mu},s}(\boldsymbol{\xi}, t - v_0^{-1}(\boldsymbol{\xi}\cdot\mathbf{x} + \zeta z)) \tag{35}$$

with $\tilde{\psi}_{\boldsymbol{\mu},s}(\boldsymbol{\xi},\tau) = \tilde{\psi}(\boldsymbol{\xi} - \boldsymbol{\xi}_\mathbf{n}, \tau - t_s + v_0^{-1}\boldsymbol{\xi}\cdot\mathbf{x_m})$ being the TD plane wave spectrum (23) of $\psi_{\boldsymbol{\mu},s}(\mathbf{x},t)$ [cf. $\hat{\tilde{\psi}}_{\boldsymbol{\mu}}(\boldsymbol{\xi})$ of (9)]. $\Psi^+_{\boldsymbol{\mu},s}(\mathbf{r},t)$ are also the inverse Fourier transform of the FD propagators $\hat{\Psi}^+_{\boldsymbol{\mu}}(\mathbf{r})$ of (9) to the time coordinate $t - ts$.

We are interested in the high-collimation parameter regime where $\Psi^+_{\boldsymbol{\mu},s}(\mathbf{r},t)$ behave like well-collimated space-time wavepackets that propagate along the $\boldsymbol{\mu}$-beam axis, with their center located at $z^+_{b_{\boldsymbol{\mu}}} = v_0(t - t_s)$ along the beam axis where t_s is the initiation time at $\mathbf{x_m}$ in the $z = 0$ plane (cf. Fig. 1). It follows that $\Psi^+_{\boldsymbol{\mu},s}(\mathbf{r},t) = \Psi^+_{\boldsymbol{\mu},0}(\mathbf{r}, t - t_s)$.

Equation (34) expresses the radiated field as a sum of PB propagators, emerging from $(\mathbf{x_m}, t_s)$ on the aperture plane and propagating in the $\boldsymbol{\xi}_\mathbf{n}$ direction (Fig. 1). As discussed in connection with the FD representation in Section II-B, the excitation amplitudes $a_{\boldsymbol{\mu},s}$, calculated via the local SST (33), sense and emphasize the local radiation properties of $u_0(\mathbf{x},t)$, and hence the formulation is *a priori* localized about the space-time skeleton of geometrical optics. Further localization is due to the fact that the $(\boldsymbol{\mu}, s)$ summation in (34) accounts only for the PB propagators that pass near the space-time observation point $(\mathbf{r},t)$. The readers are referred to the discussions and examples in [9].

VI. Pulsed-Beam Frames (PBF)

Following the FD formulation in Section III, we introduce here the PBF that extends the WRT-frame expansion of Section V from the aperture plane to the propagation domain. In Section VII, it is applied for radiation from volume sources. It also provides the mathematical foundation of the local inverse scattering theory in [16] and [17].

A. Hilbert Space of Propagating Wave-Fields

As in Section III, the theory is limited to propagating wave field. We therefore consider the Hilbert subspace $\mathbb{H}_P^\Omega$ of square integrable distributions f in $(\mathbf{x},t)$ whose spatial spectrum is limited to $|\boldsymbol{\xi}| < \xi_0 < 1$, and their temporal spectrum is constrained within Ω. Thus, recalling the definitions of $\mathbb{L}_2^\Omega$ in Section V and $\mathbb{H}_P$ in (11), we define

$$\mathbb{H}_P^\Omega = \left\{ f(\mathbf{x},t) \in \mathbb{L}_2^\Omega(\mathbb{R}^2\times\mathbb{R}) \,\middle|\, \tilde{f}(\boldsymbol{\xi},\tau) = 0 \text{ for } |\boldsymbol{\xi}| \ge \xi_0 \right\} \tag{36}$$

where $\tilde{f}$ is the SST spectrum of f as defined in (23).

B. Forward and Backward Propagating PB Frames

We start, as in Section III-B, by noting that the spectral expression (35) defines the forward propagating PB waves $\Psi^+_{\boldsymbol{\mu},s}$ for all z, while by replacing $\zeta \to -\zeta$, this expression describes backward propagation PB waves $\Psi^-_{\boldsymbol{\mu},s}$. We consider only the *propagating* PBs, tagged by the index set $\boldsymbol{\mu}_P$ defined after (11). The sets $\{\Psi^\pm_{\boldsymbol{\mu},s}(\mathbf{r},t)\}_{\boldsymbol{\mu}_P,s}$ consist of forward/backward propagating PB waves that propagate in the directions $\mathring{\boldsymbol{\kappa}}^\pm_\mathbf{n} = (\boldsymbol{\xi}_\mathbf{n}, \pm\zeta_\mathbf{n})$ along the $\boldsymbol{\mu}$ axes in Fig. 2, converging at $z = 0$ to the WRT frame set $\psi_{\boldsymbol{\mu},s}(\mathbf{x},t)$ of (30).

Likewise, we define the PB-sets $\{\Phi^\pm_{\boldsymbol{\mu},s}(\mathbf{r},t)\}_{\boldsymbol{\mu}_P,s}$ by replacing in (35) $\psi_{\boldsymbol{\mu},s}$ by $\varphi_{\boldsymbol{\mu},s}$ of (31). Clearly, the properties of these sets are similar to those of $\Psi^\pm_{\boldsymbol{\mu},s}$ discussed earlier. In particular, at $z = 0$, both converge to $\varphi_{\boldsymbol{\mu},s}$. Note that in the highly overcomplete regime used, $\Phi^\pm_{\boldsymbol{\mu},s}$ have essentially the same form as $\Psi^\pm_{\boldsymbol{\mu},s}$ [see comment after (31) and also specific expressions in (B5) and (B6)].

C. Pulsed-Beam-Frame Theorem

The following theorem is a generalization of Theorem 1 of Section III. The proof is a direct consequence of the UWB properties 1) and 2) discussed in Section II and is not given here (see [18]).

Theorem 3 (The Pulsed-Beam-Frame Theorem): Over $\mathbb{H}_P^\Omega$, the forward/backward propagating beam sets $\{\Psi^\pm_{\boldsymbol{\mu},s}(\mathbf{r},t)\}$ constitute frames at any given plane $z = const$, with $\{\Phi^\pm_{\boldsymbol{\mu},s}(\mathbf{r},t)\}$ being their canonical dual frames, respectively.

This theorem implies that any function $f(\mathbf{x},t) \in \mathbb{H}_P^\Omega$ defined over a given z plane can be expanded using either the $\Psi^+_{\boldsymbol{\mu},s}$ or the $\Psi^-_{\boldsymbol{\mu},s}$ sets at that plane. As in (12), a special case of interest is when the functions to be expanded are forward or backward propagating waves $u^\pm(\mathbf{r},t)$. In this case, it makes sense to expand them using the $\Psi^{\pm}_{\boldsymbol{\mu},s}$ set, respectively, namely,+

$$u^{\pm}(\mathbf{r},t) = \sum_{\boldsymbol{\mu}\in\boldsymbol{\mu}_P,s} A^{\pm}_{\boldsymbol{\mu},s}\Psi^{\pm}_{\boldsymbol{\mu},s}(\mathbf{r},t). \tag{37}$$

In view of the coefficient invariance, Theorem 2 and (13), the coefficients may be evaluated over any z' plane, namely (see proof in [18])

$$A^{\pm}_{\boldsymbol{\mu},s} = \left\langle u^{\pm}(\mathbf{r},t), \Phi^{\pm}_{\boldsymbol{\mu},s}(\mathbf{r},t)\right\rangle\Big|_{z'} = a^{\pm}_{\boldsymbol{\mu},s} \tag{38}$$

where $a^{\pm}_{\boldsymbol{\mu},s}$ are the coefficients calculated over the $z = 0$ plane via (33).

D. Isodiffracting Pulsed-Beam Propagators

Specifically, as noted in item 4) of Section II, we use the ID-PB set whose favorable properties are discussed there. Once the initial conditions of these propagators are defined, say at the $z = 0$, one may track them analytically in a general inhomogeneous medium [19], [20].

Explicit expressions for $\Psi^{\pm}_{\boldsymbol{\mu},s}$ and $\Phi^{\pm}_{\boldsymbol{\mu},s}$ in free space are given in (B5) and (B6). As in the FD case (Section II-C2), they depend on the collimation length b. Once b is determined by the wave modeler for a given application, the lattice parameters $(\bar{x}, \bar{\xi})$ are determined via (A2). In addition, (B5) and (B6) depend on the analytic filter functions $\stackrel{+}{\Upsilon}(t)$ that are fully determined by the bandwidth $\Omega = [\omega_{\min}, \omega_{\max}]$, and also on the parameter γ that defines the number of derivatives in $\stackrel{+}{\Upsilon}(t)$. Its role and the guidelines for choosing it are thoroughly discussed in Appendix B-C and in Table I.

VII. Pulsed-Beam Frame (PBF) Representation of Radiation From a Volume Source

As in Section IV, we demonstrate the BPF concept by considering radiation from a time-dependent source distribution $q(\mathbf{r},t)$. The field $u(\mathbf{r},t)$ satisfies the 3-D wave equation

$$\left[\nabla^2 - v_0^{-2}\partial_t^2\right]u(\mathbf{r},t) = -q(\mathbf{r},t) \tag{39}$$

where q is bounded between $z^{\pm}$, with $z^- < z^+$. The solution to (39) can be expressed by Green's function integration

$$u(\mathbf{r},t) = \int d^3r' \, \frac{q(\mathbf{r}', t - v_0^{-1}|\mathbf{r}-\mathbf{r}'|)}{4\pi|\mathbf{r}-\mathbf{r}'|}. \tag{40}$$

Here, however, we are interested with a PB expansion of the radiation. In view of (37), it has the form

$$u^{\pm}(\mathbf{r},t) = \sum_{\boldsymbol{\mu}_P,s} A^{\pm}_{\boldsymbol{\mu},s}\Psi^{\pm}_{\boldsymbol{\mu},s}(\mathbf{r},t), \quad \text{for } z \gtrless z^{\pm}. \tag{41}$$

The PB amplitudes in (41) are found by inserting $u(\mathbf{r},t)|_{z^{\pm}}$ of (40) into (38). Following a procedure similar to that in (17) and (18), we obtain

$$A^{\pm}_{\boldsymbol{\mu},s} = \int dt \int_V d^3r \, q(\mathbf{r},t)\Phi^{G\pm}_{\boldsymbol{\mu},s}(\mathbf{r},t) \tag{42a}$$

$$= \left\langle q(\mathbf{r},t), \, \Phi^{G\pm}_{\boldsymbol{\mu},s}(\mathbf{r},t)\right\rangle_V \tag{42b}$$

where Green's function-based propagators $\Phi^{G\pm}_{\boldsymbol{\mu},s}$ are the TD counterparts of $\hat{\Phi}^{G\pm}_{\boldsymbol{\mu}}(\mathbf{r})$ in (19) at the time variable $t - t_s$ [up to multiplying also by $\bar{t}$ as in (31)]. In view of (19b), they are related to $\Phi^{\pm}_{\boldsymbol{\mu},s}$ via

$$\Phi^{G\pm}_{\boldsymbol{\mu},s}(\mathbf{r},t) = \frac{-v_0}{2\cos\theta_{\mathbf{n}}}\partial_t^{-1}\Phi^{\pm}_{\boldsymbol{\mu},s}(\mathbf{r},t) \tag{43}$$

where $\cos\theta_{\mathbf{n}} = \sqrt{1 - \boldsymbol{\xi}_{\mathbf{n}}\cdot\boldsymbol{\xi}_{\mathbf{n}}}$ is the beam angle with respect to the z-axis, and ∂_t^{-1} denotes a t-integration.

Equation (42) is the main result in this section. It expresses the PB amplitudes in terms of the projection of q onto the forward/backward propagating PBs as they traverse the source (see Fig. 2). In physical terms, as the $(\boldsymbol{\mu}, s)$ PB traverses through the source q, it accumulates local contributions along its center of mass whose propagation trajectory along the $\boldsymbol{\mu}$-beam axis is $z_{b_{\boldsymbol{\mu}}} = v_0(t - t_s)$ (Fig. 2). From a mathematical perspective, the operation in (42) can be regarded as a WRT of $q(\mathbf{r},t)$ with respect to the PB window functions [16].

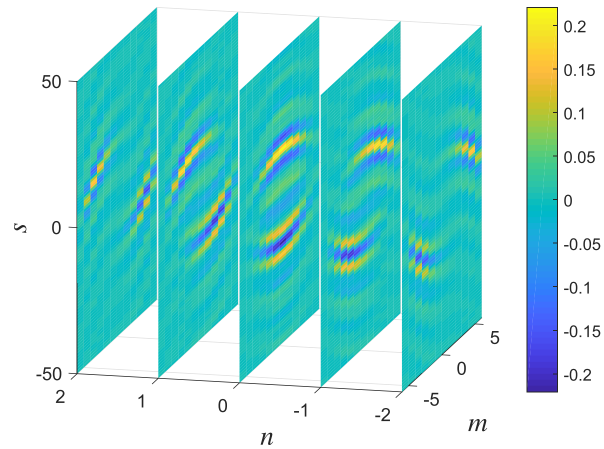

Fig. 8. Expansion coefficients $A^{+}_{\boldsymbol{\mu},s}$ in (42) for the TD source in (44).

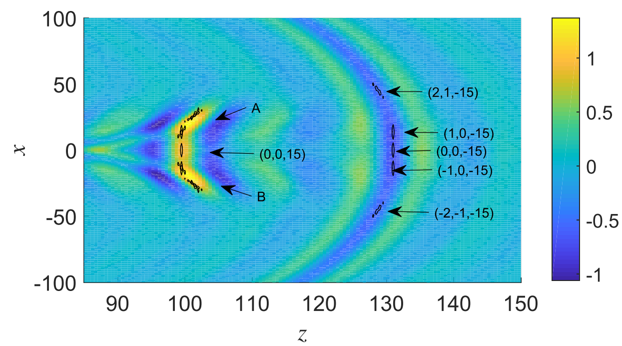

Fig. 9. Snapshot of the radiated field in the (x, z) plane at $t = 115$, calculated via the BS. To get physical insight, we also outline the footprint of the dominant PBs at some representative space-time points (dashed ellipses) and indicate in parenthesis their phase space coordinates (m, n, s) (cf. Fig. 8). The strongest peaks are obtained at points A and B where the contributing PBs at A are $(m, n, s) = (1, 0, 15)$, $(2, 1, 15)$, $(3, -1, 15)$, $(2, 0, 15)$, $(4, -2, 10)$. For points near B, the contributing beams are symmetrical, namely, $m \to -m$ and $n \to -n$.

A. Example A: A Source With an Axial Progression

We consider the 2-D source distribution $q(\boldsymbol{\rho}, t)$ which is the TD counterpart of $\hat{q}(\boldsymbol{\rho}, \omega)$ in (20), namely,

$$q(\boldsymbol{\rho},t) = q_0(t - z/v_q), \quad \text{for } |\boldsymbol{\rho}| < a \text{ and } 0 \text{ otherwise} \tag{44}$$

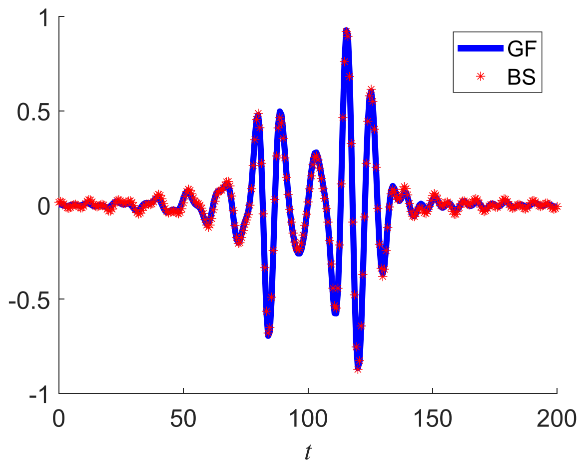

Fig. 10. TD signal on the $x = 0$ axis at $z = 100$.

where $q_0(t)$ is a short pulse whose spectrum is bounded essentially in $\mathbf{\Omega} = [\omega_{\min}, \omega_{\max}] = [0.5, 1]$, so that its pulselength $T_q \sim 2\pi$. v_q is the speed of the pulse progression, and we choose here $v_q = 0.8v_0$ with the units normalized such that $v_0 = 1$. The source support $a = 20\pi$ is large on the pulselength scale. The reference solution is calculated using the 2-D Green's function

$$G(\boldsymbol{\rho}, t; \boldsymbol{\rho}', t') = \frac{1}{2\pi} \frac{H(t - t' - R/v_0)}{\sqrt{(t - t')^2 - (R/v_0)^2}} \tag{45}$$

where $H(t)$ is the Heaviside step function and $R = |\boldsymbol{\rho} - \boldsymbol{\rho}'|$.

1) Choosing the Expansion Parameters: The beam expansion parameters $(b, \nu_{\max})$ were chosen as in the UWB-FD example of Section IV-A, giving the values of $(\bar{x}, \bar{\xi})$ as noted in Section IV-A1. For the TD problem, we also chose $\bar{t} = 1$, so that the PB are five times more localized in time than the actual data. Referring to the discussion in (29), we can use $\omega_h \approx 5$. The filter function $\overset{+}{\Upsilon}(\cdot)$ in (B5) and Fig. 13 has been chosen accordingly such that $(\omega_L, \omega_H) = (\omega_{\min}, \omega_h) = (0.5, 5)$, and $\Delta_L = \Delta_H = 0.05$. The PB propagators $\Psi^{\pm}_{\boldsymbol{\mu},s}(\boldsymbol{\rho}, t)$ and the sampling propagators $\Phi^{G\pm}_{\boldsymbol{\mu},s}$ in (42) are given by (C4)–(C10). In view of the discussion after (C10) [see also (B6)], we choose the parameters there to be $(\gamma, \alpha) = (0, 0)$ so that $\Psi^{\pm}_{\boldsymbol{\mu},s}(\boldsymbol{\rho}, t)$ are proportional to $\mathrm{Re}\overset{+}{\Upsilon}$ and are symmetrical about their center of mass and peak there, while $\Phi^{G\pm}_{\boldsymbol{\mu},s}$ are proportional to $\mathrm{Re}\overset{+}{\Upsilon}{}^{(1)}$ (convolved with $|t|^{-1/2}$) and are antisymmetric along the beam axes. It follows that these sampling kernels sense essentially the *derivative* of $q(\boldsymbol{\rho}, t)$ along the beam axis. Note that choosing any other value of $\gamma = 1, 2, 3$ and of α leads to other final result. For example, for $(\gamma, \alpha) = (0, \pi/2)$, $\Psi^{\pm}_{\boldsymbol{\mu},s}$ are antisymmetric along the beam while $\Phi^{G\pm}_{\boldsymbol{\mu},s}$ are symmetrical.

2) Expansion Coefficients: The expansion coefficients $A^{\pm}_{\boldsymbol{\mu},s}$ were calculated via (42). As noted earlier, the sampling propagators $\Phi^{G\pm}_{\boldsymbol{\mu},s}$ sense essentially the *derivative* of $q(\boldsymbol{\rho}, t)$ along the beam axis. Henceforth, we shall be interested only in the field for $z > z^+$, described by the forward propagating PBF $\Psi^{+}_{\boldsymbol{\mu},s}$. The resulting coefficients $A^{+}_{\boldsymbol{\mu},s}$ are shown in Fig. 8. For clarity, we depict only the coefficients in the range $|m| \le 6$, $|n| \le 2$, and $|s| \le 50$, corresponding to the physical coordinates range $|x_m| < 82.4$, $|\theta_n| < 16°$ and $|t_s| < 50$.

Strong excitation coefficients are obtained for the $(\boldsymbol{\mu}, s)$ PBs that best match the *local phase-space distribution* of $q(\boldsymbol{\rho}, t)$. In the present example, there are mainly two mechanisms that give rise to strong coefficients. The first is due to PBs that follow the source-pulse q_0 as it traverses the medium. Recalling that the propagation trajectory of q_0 is $z = vt$, while the propagation trajectories of $\Phi^{G+}_{\boldsymbol{\mu},s}$ are $z_{b_\mu} = v_0(t - t_s)$ along the $\boldsymbol{\mu}$ beam axis is $z_{b_\mu} = z/\zeta_n$ with $\zeta_n = \cos\theta_n = \sqrt{1 - \xi_n^2}$, it follows that the PBs that track the center of q_0 are described by $\zeta_n v_0 \approx v$, $t_s \approx 0$ with $|x_m| < a$. Substituting the values of v/v_0 and $\bar{\xi}$, we obtain $n \approx \pm 4$. In fact, recalling that the sampling kernel $\Phi^{G+}_{\boldsymbol{\mu},s}$ senses essentially the *derivative* of $q(\boldsymbol{\rho}, t)$ along the beam axis, the contributions of the peak of q_0 (i.e., the $s = 0$ term) are weak, and the strongest coefficients $A^{+}_{\boldsymbol{\mu},s}$ are obtained where q_0 has a strongest derivative, i.e., for $|t_s| \sim T_q/2 \sim \pi$ where T_q is the pulselength of q_0. In any case, these coefficients are significantly weaker than those corresponding to the source truncation at $\rho = a$ that are discussed next.

The other, and in this example more significant, mechanism that generates strong excitation coefficients is the source truncation at $\rho = a$ (recall that the expansion parameters were chosen such that $\Phi^{G\pm}_{\boldsymbol{\mu},s}$ sense essentially the *derivative* of $q(\boldsymbol{\rho}, t)$ along the beam axis). As an example, we consider the contribution of the $(m, n) = (0, 0)$ PBs whose propagation trajectories along the z-axis are given by $t - t_s = z/v_0$. It follows that the PB that reaches the truncation point $z = a$ at the time a/v at which the source-pulse q_0 reaches that point, is tagged by $t_s \approx a/v - a/v_0$. In the present example, setting $v = 0.8v_0$ and $a = 20\pi$, we obtain $t_s \approx 5\pi$. Likewise, the contribution from the source truncation at $z = -a$ is described by $t_s \approx -5\pi$. These contributions are readily observed in Fig. 8. One also observes that the edge truncation contribution to beams with $n = 0$ but $|m| \ge 1$ has a smaller $|t_s|$, due to the fact that q_0 reaches the corresponding truncation points at $|t| < a/v$. Similar arguments can be used to explain the coefficients for the tilted beams with $n \ne 0$.

3) Beam-Summation Calculation of the Field: Fig. 9 depicts a snapshot of the radiating field at $t = 115$, which was calculated via the BS approach (41). To check the accuracy of these results, we depict in Fig. 10, the signal at $z = 100$ on the $x = 0$ axis, observing an excellent agreement with the reference solution calculated via Green's function integration.

The BS provides a local physical insight into the structure of the field. The dashed ellipses in Fig. 9 depict the footprints of the dominant PBs at some representative point, along with their phase-space coordinates (m, n, s) (cf. Fig. 8). Note that the leading edge of the field (around $z = 130$) is generated by PBs with index $s = -15$, corresponding to contributions from the region $(x, z) = (0, -a)$ in the source domain, whereas the trailing edge (around $z = 100$) is generated by PBs with index $s = 15$, corresponding to contributions from the region $(x, z) = (0, a)$ in the source domain. The strongest peak at point A is a sum of PBs with indexes $(m, n, s) = (1, 0, 15)$, $(2, 1, 15)$, $(3, -1, 15)$, $(2, 0, 15)$, $(4, -2, 10)$, corresponding to the physical coordinates: $(x_m, \theta_n, t_s) \approx (13.7, 0, 15)$, $(27.4, -8, 15)$, $(41.2, -8, 15)$, $(27.4, 0, 15)$, and $(54.9, -16, 10)$. For the

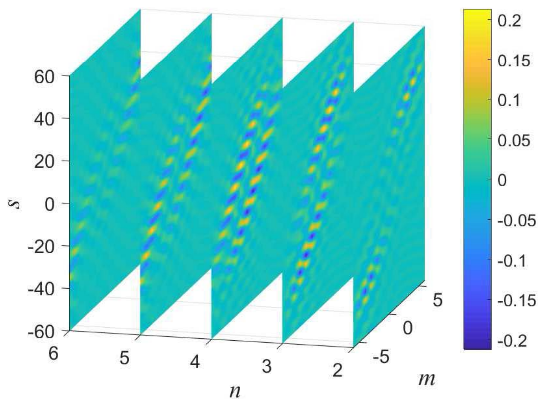

Fig. 11. Expansion coefficients $A^{+}_{\boldsymbol{\mu},s}$ for the TD source in (46).

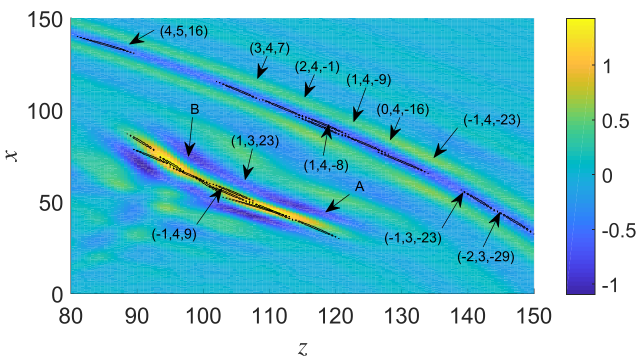

Fig. 12. Snapshot of the radiated field in the (x, z) plane at $t = 32.79$, calculated via the BS. To get physical insight, we also outline the footprint of the dominant PBs at some representative space-time points (dashed ellipses) and indicate in parenthesis their phase space coordinates (m, n, s) (cf. Fig. 11). The strongest peaks are obtained at points A and B where the contributing PBs at A are $(m, n, s) = (-2, 4, 1)$, $(-1, 4, 8)$, $(-3, 4, -7)$, $(-4, 5, -16)$. For points near B, the contributing beams are $(2, 3, 29)$, $(0, 4, 16)$, $(3, 3, 34)$, $(1, 4, 23)$.

symmetrical point B, the contributing beams are obtained by replacing $m \to -m$ and $n \to -n$.

B. Example B: A Source With an Oblique Forward/Backward Progression

Finally, we consider the TD counterpart of the example in (21), namely,

$$q(\boldsymbol{\rho}, t) = q_0(t - \mathring{\boldsymbol{\kappa}}_q \cdot \boldsymbol{\rho}/v_q) + q_0(t + \mathring{\boldsymbol{\kappa}}_q \cdot \boldsymbol{\rho}/v_q) \qquad (46)$$

where the first and second terms, henceforth referred to as $q^{\pm}$, respectively, represent sources which progress at speed v_q in the positive or negative $\mathring{\boldsymbol{\kappa}}_q$ direction, with $\mathring{\boldsymbol{\kappa}}_q = (\sin\theta_q, \cos\theta_q)$. $q_0(t)$ is the short pulse discussed in (44). In the following numerical example, we have $\theta_q = 30°$ and $v_q = 0.8v_0$ and calculate the radiated filed at $z = 100$.

We consider the radiation into the half-space $z > 0$ where the field is expressed in terms of forward propagating beam set $\Psi^{+}_{\boldsymbol{\mu},s}$ as in (41). We employ the same expansion parameters as in the examples in Section VII-A. The respective amplitudes $A^{+}_{\boldsymbol{\mu},s}$ in Fig. 11 are the combined contributions of q^+ and q^-: we do not show them separately since the latter are negligible (see Fig. 5). The coefficients shown are in the range $|m| \le 6$, $2 \le n \le 6$, and $|s| \le 60$, corresponding to the physical coordinates range $|x_m| < 82.83$, $15.94 < \theta_n < 55.47°$ and $|t_s| < 60$. They are identified as contributions of the forward propagating pulse q^+ in (46). Following the same considerations as in Section VII-A2, one readily concludes that the dominant terms are $n = 5$ [see also the corresponding FD example in Section IV-B and Fig. 5(a)]. In addition, strong contributions are obtained for beams that sense the discontinuity along the boundary of the source, tagged here by $n = 4$ corresponds to $\theta_{\mathbf{n}} = 33.31°$.

Finally, in Fig. 12 we depict a snapshot of the radiated field in the (x, z) plane at $t = 132.8$. As in Fig. 9, the dominant PBs are shown as dashed ellipses along with their phase-space coordinates (m, n, s). At point A, these coordinates are $(-2, 4, 1)$, $(-1, 4, 8)$, $(-3, 4, -7)$, and $(-4, 5, -16)$. At point B, they are (m, n, s) values are $(2, 3, 29)$, $(0, 4, 16)$, $(3, 3, 34)$, and $(1, 4, 23)$. Note that the dominant terms are due to the source discontinuities corresponding to the direction of the source pulse.

VIII. Conclusion

We presented two novel BS schemes for radiation from time-harmonic or time-dependent volume source distributions, where the field is expanded using discrete phase-space sets of beam waves. Consequently, this paper consists of two parts: Sections II–IV deal with the UWB-FD formulation, while Sections V–VII deal with the TD formulation.

The beam sets are illustrated in Fig. 2, which depicts both the time-harmonic ID-GB $\{\hat{\Psi}^{\pm}_{\boldsymbol{\mu}}(\mathbf{r})\}$ (hatched arrows) and the time-dependent ID-PB propagators $\{\Psi^{\pm}_{\boldsymbol{\mu},s}(\mathbf{r}, t)\}$ (small ellipses). These sets are structured upon a frequency-independent beam lattice, identified by the initiation points $\mathbf{x_m}$, directions $\boldsymbol{\xi}_{\mathbf{n}}$ and times t_s over the $z = 0$ plane, as defined in (3) and (28). The criteria for choosing the unit-cell dimensions $(\bar{x}, \bar{\xi}, \bar{t})$ have been discussed in (4), (10), (A2), and (29), and demonstrated in the examples of Sections IV-A and IV-B and Sections VII-A and VII-B. Explicit expressions for the ID-GB and for the ID-PB frame elements are given in Appendixes A and B for the 3-D FD and TD formulations, respectively, and in Appendix C for 2-D formulations where the TD Green's function introduces fractional derivatives.

Theorems 1 and 3 establish that FD and the TD beam sets $\{\hat{\Psi}^{\pm}_{\boldsymbol{\mu}}(\mathbf{r})\}$ and $\{\Psi^{\pm}_{\boldsymbol{\mu},s}(\mathbf{r}, t)\}$ constitute frames, termed "BFs," not only over the aperture plane, where they reduce to the conventional WFT and WRT frame sets in [2] and [9], respectively, but actually *everywhere* in the propagation domain. Consequently, they can be used to expand radiation from volume source distributions and not only from aperture sources as was done so far. We have also constructed the *dual* BFs.

The final expression for the beam expansion of radiation from volume source is given in (16) and (41) for the UWB-FD and TD formulations, respectively, wherein (18) and (42) express the expansion amplitudes in terms of the projection of the volume sources onto the forward/backward propagating *dual* beam waves as they traverse the source (see Fig. 2). As such, these formulations provide local generalizations to the conventional plane waves or Green's function formulations, which resolve the local features of the source distributions in space time, as demonstrated by the examples in Sections IV-A and IV-B and Sections VII-A and VII-B. In these detailed examples, we also explained the considerations for choosing the expansion parameters, namely, the phase-space lattices, the beam parameters, and the filter functions $e^{i\alpha}\overset{+}{\Upsilon}^{(\gamma)}(t)$ that are used in the TD formulation [see (B5)–(B6), (C4)–(C5), and discussions thereafter].

As demonstrated, the beam formulations capture the main physics and express the field using a relatively few terms. These properties have been used to study wave propagation through randomly fluctuating medium [12], [13] and for local tomographic inverse scattering [16], [17].

Appendix A
Explicit Expressions for the Isodiffracting Gaussian Beams (ID-GB)

The ID windows are Gaussian-type windows whose width is scaled with the frequency in a specific fashion, termed ID that renders the favorable properties listed in items 2)–4) in Section II. The ID windows have the general form [1]

$$\hat{\psi}_{\mathrm{ID}}(x) = e^{-|k|\mathbf{x}\cdot\mathbf{x}/2b} \tag{A1}$$

where $b > 0$ is a frequency-independent parameter, whose *optimal* value for the present application is discussed in the following. This parameter will be identified in (A4)–(A5) as the *collimation* or *Rayleigh* length of the GB that emerges from this window.

For a snug frame, it is required that the window will be matched to the phase-space lattice $(\bar{x}, \bar{\xi})$ in the sense that the spatial and spectral coverage of the window are balanced, i.e., $\Delta_x/\bar{x} = \Delta_\xi/\bar{\xi}$ where Δ_x and Δ_ξ are the spatial and spectral widths of $\hat{\psi}_{\mathrm{ID}}$, giving $b_{\mathrm{snug}} = \bar{x}/\bar{\xi}$ [2, eq. 33]. Note that this b provides a snug frame for all ω. Combining this relation with (4) implies that once b is determined for a given application then the *optimal* values for the beam lattice are

$$(\bar{x},\ \bar{\xi}) = \sqrt{2\pi\nu_{\max}/k_{\max}}\,(b^{1/2},\ b^{-1/2}) \tag{A2}$$

where $\nu_{\max}$ is the value of ν at the highest frequency $k_{\max}$ and is typically taken to be $\nu_{\max} \simeq 1/3$ as noted in (7). b is typically chosen to match the propagation environment, but it should also satisfy the collimation condition $bk_{\min} \gg 1$ at the lowest frequencies. Further considerations for choosing b and $\nu_{\max}$ are discussed in [2, Secs. IV-B and V-A].

Using (7), the dual ID window is given, approximately, by

$$\hat{\varphi}_{\mathrm{ID}}(\mathbf{x}) \simeq \left(\nu_{\max}^2/\pi b k_{\max}^2\right) k^3\, \hat{\psi}_{\mathrm{ID}}(\mathbf{x}). \tag{A3}$$

The forward/backward propagating phase-space propagators are calculated by substituting $\tilde{\hat{\psi}}_{\mathrm{ID}}$ into (9). For large kb, one obtains the GB form [2, Sec. IV-A]

$$\hat{\Psi}^{\pm}_{\boldsymbol{\mu}}(\mathbf{r}) \simeq \sqrt{\frac{-iF_{\boldsymbol{\mu}1}}{z_{b_\mu} - iF_{\boldsymbol{\mu}1}}\,\frac{-iF_{\boldsymbol{\mu}2}}{z_{b_\mu} - iF_{\boldsymbol{\mu}2}}} \times \exp\left\{ik\left[z_{b_\mu} + \frac{x_{b_{\mu 1}}^2/2}{z_{b_\mu} - iF_{\boldsymbol{\mu}1}} + \frac{x_{b_{\mu 2}}^2/2}{z_{b_\mu} - iF_{\boldsymbol{\mu}2}}\right]\right\} \tag{A4}$$

where $(z_{b_\mu},\ \mathbf{x}_{b_\mu})$ are the beam coordinates along and transverse to the beam axes, respectively (see Figs. 1 and 2), and $\mathbf{x}_{b_\mu} = (x_{b_{\mu1}}, x_{b_{\mu2}})$ are chosen such that the unit vector $\mathring{\boldsymbol{x}}_{b_{\mu1}}$ lies in the plane spanned by $\mathring{\boldsymbol{z}}$ and $\boldsymbol{\xi}_{\mathbf{n}}$, and $\mathring{\boldsymbol{x}}_{b_{\mu2}} = \mathring{\boldsymbol{z}}_{b_\mu} \times \mathring{\boldsymbol{x}}_{b_{\mu1}}$ [2, eq. 28]. In (A4)

$$F_{\boldsymbol{\mu}1} = b\cos^2\theta_{\mathbf{n}}, \quad F_{\boldsymbol{\mu}2} = b. \tag{A5}$$

Expression (A4) has the standard form of a GB that propagates along the z_{b_μ}-axis with $F_{\boldsymbol{\mu}_\ell}$, $\ell = 1, 2$, being the collimation lengths in the planes spanned by $(\mathring{z}_{b_\mu}, \mathring{x}_{b_{\mu\ell}})$. As discussed after (A1), $F_{\boldsymbol{\mu}1,2}$ are frequency independent, hence the ID designation. For more details on the ID-GB, please refer to [1]. Separating the phase in (A4) into real and imaginary parts, one finds that the beamwidths $W_{\boldsymbol{\mu}\ell}(z_b)$ in the ℓ plane, where the field intensity reduces to e^{-1}, are given as

$$W_{\boldsymbol{\mu}\ell}(z_b) = W_{0_{\mu\ell}}\sqrt{1+(z_{b_\mu}/F_{\boldsymbol{\mu}\ell})^2},\ \ W_{0_{\mu\ell}} = \sqrt{F_{\boldsymbol{\mu}\ell}/k}. \tag{A6a}$$

For $z_{b_\mu} < F_{\boldsymbol{\mu}\ell}$, the beamwidths are essentially $W_{0_{\mu\ell}}$, whereas for $z_{b_\mu} > F_{\boldsymbol{\mu}\ell}$, they diffract in the respective planes at angles

$$\Theta_{\boldsymbol{\mu}\ell} = 1/\sqrt{kF_{\boldsymbol{\mu}\ell}}. \tag{A6b}$$

Finally, in view of (A3), the dual propagators are given as

$$\hat{\Phi}^{\pm}_{\boldsymbol{\mu}}(\mathbf{r}) \simeq \left(\nu_{\max}^2/\pi b k_{\max}^2\right) k^3\, \hat{\Psi}^{\pm}_{\boldsymbol{\mu}}(\mathbf{r}) \tag{A7}$$

and [see (19b)]

$$\hat{\Phi}^{G\pm}_{\boldsymbol{\mu}}(\mathbf{r}) \simeq \left(-i\nu_{\max}^2/2\pi b k_{\max}^2 \cos\theta_{\mathbf{n}}\right) k^2\, \hat{\Psi}^{\pm}_{\boldsymbol{\mu}}(\mathbf{r}). \tag{A8}$$

Appendix B
Explicit Expressions for the Isodiffracting Pulsed Beam (ID-PB)

A. “Mother” Windows

The ID-PB windows are the TD counterparts of the ID-GB windows used in the FD formulation. Their frequency spectra are obtained by multiplying the ID-GB windows of (A1) and (A3) by arbitrary spectra $\hat{f}(\omega)$ and $\hat{g}(\omega)$, respectively, namely,

$$\hat{\psi}_{\mathrm{ID}}(\mathbf{x}) \to \hat{f}(\omega)\hat{\psi}_{\mathrm{ID}}(\mathbf{x}), \quad \hat{\varphi}_{\mathrm{ID}}(\mathbf{x}) \to \hat{g}(\omega)\hat{\varphi}_{\mathrm{ID}}(\mathbf{x}). \tag{B1}$$

In order to have a valid dual set at all frequencies in the pertinent FD, it is required that $\hat{f}(\omega)\hat{g}^*(\omega) = 1$, for $\omega \in \boldsymbol{\Omega}$, while for $\omega \not\in \boldsymbol{\Omega}$, they can be chosen quite arbitrarily. They are chosen such that they taper smoothly to zero, thus yielding smooth and localized spatiotemporal windows. The considerations for choosing f, g are discussed in Sec. B.

The TD counterpart of ψ_{ID} is obtained by inverting (B1) into the TD. Since $\hat{\psi}_{\mathrm{ID}}$ has different analytic form for positive and negative ω, we use the analytic signal formulation in (24)–(25). Thus, applying (24) to (B1), we obtain the TD windows

$$\psi_{\mathrm{ID}}(\mathbf{x}, t) = \mathrm{Re}\overset{+}{f}(t - i|\mathbf{x}|^2/2bv_0). \tag{B2}$$

The space-time properties of ψ_{ID} are governed by the filter f. The temporal windowing is due to the pulse shape of $\overset{+}{f}(t)$, while the spatial $\mathbf{x}$-windowing is due to the negative imaginary part of the argument of $\overset{+}{f}$ in (B2), which increases quadratically with $|\mathbf{x}|$, and due to the general property of analytic signals, which decay as the imaginary part of their argument becomes more negative (see (24)). Assuming that

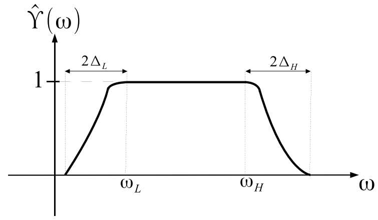

Fig. 13. Frequency characterization of a generic filter.

the pulselength of $f(t)$ is $\sim T_f$, it follows that this is also the temporal support of ψ_{ID}, while the spatial width in $|\mathbf{x}|$ is of order $\sim \sqrt{v_0 T_f b}$ [1], [19]. Note that the argument of $\overset{+}{f}$ has a negative imaginary part as required by (24).

The dual window is given by using the relation in (A3), giving

$$\varphi_{\text{ID}}(\mathbf{x}, t) = \frac{\nu_{\max}^2}{\pi b v_0 \omega_{\max}^2} \mathrm{Re}\{-i \overset{+}{g}^{(3)}(t - i|\mathbf{x}|^2/2bv_0)\} \quad \text{(B3)}$$

where the parenthesized superscript (n) denotes the nth derivative of a function with respect to its argument.

B. Constructing the Filters f and g

Following [9], we use a class of analytic filters that are derived from the standard analytic filter $\overset{+}{\Upsilon}(t)$ whose frequency spectrum $\hat{\Upsilon}(\omega)$ is characterized by four parameters as defined in Fig. 13 (after [9, Fig. 4]): 1) the operative frequency band ω_L, ω_H where $\hat{\Upsilon}(\omega) = 1$; and 2) the lower and upper transition zones $2\Delta_L$, $2\Delta_H$ where $\hat{\Upsilon}$ tappers smoothly to zero in order to obtain smooth and localized windows.

Given the signal bandwidth $\mathbf{\Omega}$, we choose ω_L, ω_H such that $\mathbf{\Omega} \subseteq [\omega_L, \omega_H]$, while typically we choose an equality. The transition parameters Δ_L and Δ_H are then determined such that larger transition zones lead to smoother and more localized windows but, as implied by (29), require higher sampling rate.

Explicit expressions for $\overset{+}{\Upsilon}(t)$ with linear and cubic tapers are given in [9, eqs. (32)]. Basically, $\overset{+}{\Upsilon}(t)$ is localized about $t = 0$ such that its real and imaginary parts are symmetrical and antisymmetric about $t = 0$, respectively.

The filters $\hat{f}$ and $\hat{g}$ in (B1) are taken now to be

$$\hat{f} = (-i\omega)^{\gamma} e^{i\alpha} \hat{\Upsilon}, \quad \hat{g} = (i\omega)^{-\gamma} e^{i\alpha} \hat{\Upsilon} \quad \text{(B4)}$$

where the parameters α and $\gamma \geq 0$ are added to gain flexibility, as explained in the following. Clearly, (B4) satisfies the requirement $\hat{f}(\omega)\hat{g}^*(\omega) = 1$ for $\omega \in \mathbf{\Omega}$ discussed after (B1).

Multiplying (A4) by $\hat{f}$ of (B4) and inverting the result into the TD using the analytic signal formulation, yields

$$\Psi_{\boldsymbol{\mu},s}(\mathbf{r}, t) = \mathrm{Re}\left\{ \sqrt{\frac{-iF_{\boldsymbol{\mu}1}}{z_{b_{\boldsymbol{\mu}}} - iF_{\boldsymbol{\mu}1}} \frac{-iF_{\boldsymbol{\mu}2}}{z_{b_{\boldsymbol{\mu}}} - iF_{\boldsymbol{\mu}2}}} \right.$$
$$\left. \times e^{i\alpha} \overset{+}{\Upsilon}^{(\gamma)} \left(t - t_s - \frac{z_{b_{\boldsymbol{\mu}}}}{v_0} - \frac{x_{b_{\boldsymbol{\mu}1}}^2/2v_0}{z_{b_{\boldsymbol{\mu}}} - iF_{\boldsymbol{\mu}1}} - \frac{x_{b_{\boldsymbol{\mu}2}}^2/2v_0}{z_{b_{\boldsymbol{\mu}}} - iF_{\boldsymbol{\mu}2}} \right) \right\} \quad \text{(B5)}$$

where, as noted after (B3), $\overset{+}{\Upsilon}^{(\gamma)}(t) \overset{\text{def}}{=} \partial_t^{\gamma} \overset{+}{\Upsilon}(t)$.

Expression (B5) has the standard form of an ID-PB, a *space-time wavepacket* that propagates along the $z_{b_{\boldsymbol{\mu}}}$ axis, with $F_{\boldsymbol{\mu}1,2}$ being the collimation lengths. As discussed after (B2), the wavepacket confinement along the beam axis is due to the pulse shape of $\overset{+}{\Upsilon}(t)$, while the transversal confinement in $\mathbf{x}_{b_{\boldsymbol{\mu}}}$ is due to the negative imaginary part of the argument of $\overset{+}{\Upsilon}$ in (B5), which increases quadratically with $|\mathbf{x}_{b_{\boldsymbol{\mu}}}|$, and the general property of analytic signals that decay as the imaginary part of their argument becomes more negative. For more details on the ID-PB, refer to [1], [19].

Likewise, the dual-frame propagators $\Phi_{\boldsymbol{\mu},s}^{\pm}(\mathbf{r}, t)$ and $\Phi_{\boldsymbol{\mu},s}^{G\pm}(\mathbf{r}, t)$ are obtained by multiplying $\hat{\Phi}_{\boldsymbol{\mu}}^{\pm}(\mathbf{r})$ and $\hat{\Phi}_{\boldsymbol{\mu}}^{G\pm}(\mathbf{r})$ of (A7) and (A8) by $\hat{g}$ of (B4) [multiplying also by $\bar{t}$ as in (31)] and inverting the result to the TD. The result has the same form as in (B5) with the replacement

$$\overset{+}{\Upsilon}^{(\gamma)}(\cdot) \longrightarrow \begin{cases} \dfrac{(-1)^{\gamma+1} \bar{t}\, \nu_{\max}^2}{\pi b v_0 \omega_{\max}^2} i \overset{+}{\Upsilon}^{(3-\gamma)}(\cdot), & \text{for } \Phi_{\boldsymbol{\mu},s}^{\pm} \\ \dfrac{(-1)^{\gamma} \bar{t}\, \nu_{\max}^2}{2\pi b \omega_{\max}^2 \cos\theta_{\mathbf{n}}} i \overset{+}{\Upsilon}^{(2-\gamma)}(\cdot), & \text{for } \Phi_{\boldsymbol{\mu},s}^{G\mp}. \end{cases} \quad \text{(B6)}$$

C. Choosing the Filter Parameters α and γ

The role of γ is to split the derivatives of $\overset{+}{\Upsilon}$ between Ψ and Φ while maintaining the condition $\hat{f}(\omega)\hat{g}^*(\omega) = 1$ for $\omega \in \mathbf{\Omega}$. For $\gamma = 0$, for example, $\Psi \sim \Upsilon$, while $\Phi \sim \Upsilon^{(3)}$, so that Φ is narrower but more oscillatory than Ψ. The choice of γ depends on the application, recalling that Φ is used to process the data (extracting the expansion coefficients) while Ψ are the propagators.

The role of the phase parameter $e^{i\alpha}$ is to control the balance between the real and imaginary parts of $\overset{+}{\Upsilon}(t)$ such that the *real windows* Ψ and Φ will have the desired properties (for example, as will be shown in the following, the wave modeler may require that these wavepackets will peak at their centers). Following the discussion that preceded (B4), we note that for even γ, $\mathrm{Re}\{\overset{+}{\Upsilon}^{(\gamma)}(t)\}$ is symmetric about its peak at $t = 0$, while for odd γ, it is antisymmetric with a null at $t = 0$. These characteristics are reversed for $\mathrm{Re}\{i\overset{+}{\Upsilon}^{(\gamma)}(t)\}$, namely, this function is symmetric or antisymmetric about $t = 0$ for odd or even γ, respectively.

These considerations are applied now to analyze the real propagators $\Psi_{\boldsymbol{\mu},s}^{\pm}$, $\Phi_{\boldsymbol{\mu},s}^{\pm}$, and $\Phi_{\boldsymbol{\mu},s}^{G\pm}$ and to choose the parameters so that they have the desired properties. We consider first points $\mathbf{r}$ in the beam collimation zone where $z_{b_{\boldsymbol{\mu}}} \ll F_{\boldsymbol{\mu}\ell}$ where $F_{\boldsymbol{\mu}\ell}$ are given in (A5). In this zone, the square root in (B5) is ~ 1 so that from (B5) and (B6) we obtain that, up to certain *real* multiplication constants, $\Psi_{\boldsymbol{\mu},s}^{\pm} \sim \mathrm{Re}\{e^{i\alpha}\overset{+}{\Upsilon}^{(\gamma)}\}$, $\Phi_{\boldsymbol{\mu},s}^{\pm} \sim \mathrm{Re}\{i\, e^{i\alpha}\overset{+}{\Upsilon}^{(3-\gamma)}\}$ and $\Phi_{\boldsymbol{\mu},s}^{G\pm} \sim \mathrm{Re}\{i\, e^{i\alpha}\overset{+}{\Upsilon}^{(2-\gamma)}\}$. It follows that if we use $\gamma = 0$ or 2 with $\alpha = 0$, or $\gamma = 1$ with $\alpha = \pi/2$, then the ID-PB's $\Psi_{\boldsymbol{\mu},s}^{\pm}$ and $\Phi_{\boldsymbol{\mu},s}^{\pm}$ are essentially symmetrical along the axis about their center of mass, whereas $\Phi_{\boldsymbol{\mu},s}^{G\pm}$ is essentially antisymmetric along its axis about its center of mass. These properties are reversed if we use instead $\gamma = 0$ or 2 with $\alpha = \pi/2$ or $\gamma = 1$ with $\alpha = 0$.

As z increases, however, the structures of the *real* propagators are gradually changing since the argument of the

TABLE I
PROPERTIES OF THE 3-D WAVEPACKETS

	even γ and $\alpha=0$, or odd γ and $\alpha=\pi/2$	odd γ with $\alpha=0$, or even γ with $\alpha=\pi/2$
$\Psi^{\pm}_{\boldsymbol{\mu},s}(\mathbf{r},t)$ near zone	symmetrical	anti-symmetrical
$\Psi^{\pm}_{\boldsymbol{\mu},s}(\mathbf{r},t)$ far zone	anti-symmetrical	symmetrical
$\Phi^{\pm}_{\boldsymbol{\mu},s}(\mathbf{r},t)$ near zone	symmetrical	anti-symmetrical
$\Phi^{G\pm}_{\boldsymbol{\mu},s}(\mathbf{r},t)$ near zone	anti-symmetrical	symmetrical

complex square root in (B5) is gradually changing until at $z_{b_\mu} \gg F_{\mu\ell}$ it becomes $\sim -i$. These considerations affect only the propagators $\Psi^{\pm}_{\boldsymbol{\mu},s}$ that are used to propagate the field from the near to the far zone, where they behave like $\Psi^{\pm}_{\boldsymbol{\mu},s} \sim \mathrm{Re}\{i\, e^{i\alpha} \overset{+}{\Upsilon}{}^{(\gamma)}\}$. They are typically irrelevant for $\Phi^{\pm}_{\boldsymbol{\mu},s}$ and $\Phi^{G\pm}_{\boldsymbol{\mu},s}$ which are used only to process the data [i.e., to calculate the expansion coefficients as in (42b)] so that by choosing b to be sufficiently larger than the source support (for example $b > z^+ - z^-$), the structure of $\Phi^{\pm}_{\boldsymbol{\mu},s}$ and $\Phi^{G\pm}_{\boldsymbol{\mu},s}$ will practically not change in the source support. For concreteness, these properties are summarized in Table I.

APPENDIX C
EXPLICIT EXPRESSIONS FOR THE ID FRAME ELEMENTS IN 2-D CONFIGURATIONS

The beam-based processing examples in this paper (Sections IV-A and IV-B and Sections VII-A and VII-B) are presented in 2-D configurations. We, therefore, summarize the relevant modifications in the 3-D-ID frame elements presented in Appendixes A and B. As will be shown, the 2-D TD expressions are somewhat different than those in 3-D as follows from the tail of the TD Green's function in (45).

2-D configurations are important not only because of their reduced numerical complexity but also since many real-world surveys of 3-D configurations are actually linear scans in one space coordinate, so that the data are processed by assuming no variations in the third coordinate (the so-called 2.5-D approach). This approach will actually be used in the examples of the beam-based inverse scattering in [16] and [17].

A. FD Formulations

The 2-D phase-space propagators $\hat{\Psi}^{\pm}_{\boldsymbol{\mu}}(\boldsymbol{\rho})$ are obtained by eliminating all the terms involving the coordinate $x_{b_{\mu 2}}$ in the 3-D ID-GB (A4), namely,

$$\hat{\Psi}^{\pm}_{\boldsymbol{\mu}}(\boldsymbol{\rho}) \simeq \sqrt{\frac{-iF_{\mu}}{z_{b_\mu} - iF_{\mu}}} \exp\left\{ik\left[z_{b_\mu} + \frac{x_{b_\mu}^2/2}{z_{b_\mu} - iF_{\mu}}\right]\right\} \tag{C1}$$

where $\boldsymbol{\rho} = (x, z)$ as in (20), and referring to (A4) and (A5), $x_{b_{\mu 1}} \to x_{b_\mu}$ and $F_{\mu 1} \to F_{\mu}$. Following (A7) and (A8), the dual-frame propagators are given as

$$\hat{\Phi}^{\pm}_{\boldsymbol{\mu}}(\boldsymbol{\rho}) \simeq (\nu_{\max}/\sqrt{\pi\, b\, v_0}\,\omega_{\max})\omega^{3/2}\hat{\Psi}^{\pm}_{\boldsymbol{\mu}}(\boldsymbol{\rho}) \tag{C2}$$

$$\hat{\Phi}^{G\pm}_{\boldsymbol{\mu}}(\boldsymbol{\rho}) \simeq (-i\nu_{\max}/2\sqrt{\pi\, b/v_0}\,\omega_{\max}\cos\theta_n)\omega^{1/2}\hat{\Psi}^{\pm}_{\boldsymbol{\mu}}(\boldsymbol{\rho}). \tag{C3}$$

B. TD Formulations

The TD propagators $\Psi^{\pm}_{\boldsymbol{\mu},s}(\boldsymbol{\rho}, t)$ are obtained, as in (B1), by multiplying $\hat{\Psi}^{\pm}_{\boldsymbol{\mu}}(\boldsymbol{\rho})$ of (C1) by $\hat{f}(\omega)$ of (B4) and inverting the result into the TD. The result is [cf. (B5)]

$$\Psi_{\boldsymbol{\mu},s}(\mathbf{r},t) = \mathrm{Re}\left\{\sqrt{\frac{-iF_{\mu}}{z_{b_\mu} - iF_{\mu}}} \times e^{i\alpha}\overset{+}{\Upsilon}{}^{(\gamma)}\left(t - t_s - \frac{z_{b_\mu}}{v_0} - \frac{x_{b_\mu}^2/2v_0}{z_{b_\mu} - iF_{\mu}}\right)\right\}. \tag{C4}$$

Likewise, the dual-frame propagators are obtained by multiplying $\hat{\Phi}^{\pm}_{\boldsymbol{\mu}}(\boldsymbol{\rho})$ and $\hat{\Phi}^{G\pm}_{\boldsymbol{\mu}}(\boldsymbol{\rho})$ of (C2) and (C3) by $\hat{g}$ of (B4) and inverting the result to the TD using also the replacement $\omega^{-1/2} \to e^{-i\frac{\pi}{4}}(-i\omega)^{-1/2}$. The result has the same form as $\Psi^{\pm}_{\boldsymbol{\mu},s}$ of (C4) with the replacement

$$\overset{+}{\Upsilon}{}^{(\gamma)}(\cdot) \to \begin{cases} \dfrac{(-1)^{\gamma+1}\bar{t}\,\nu_{\max}}{\sqrt{\pi b v_0}\,\omega_{\max}}\, e^{-i\frac{\pi}{4}}\overset{+}{\Upsilon}{}^{(\frac{3}{2}-\gamma)}(\cdot), & \text{for } \Phi^{\pm}_{\boldsymbol{\mu},s} \\ \dfrac{(-1)^{\gamma}\,\bar{t}\,\nu_{\max}}{2\sqrt{\pi b/v_0}\,\omega_{\max}\cos\theta_n}\, e^{-i\frac{\pi}{4}}\overset{+}{\Upsilon}{}^{(\frac{1}{2}-\gamma)}(\cdot), & \text{for } \Phi^{G\pm}_{\boldsymbol{\mu},s}. \end{cases} \tag{C5}$$

These expressions involve fractional time derivatives due to the $\omega^{1/2}$ terms in (C2) and (C3). For a given integer N, this operation is defined via the analytic signal representation

$$e^{-i\frac{\pi}{4}}\overset{+}{\Upsilon}{}^{(N-\frac{1}{2})}(t) \overset{\text{def}}{=} \left[\overset{+}{\Upsilon}{}^{(N)} \otimes \mathrm{Re}\left\{e^{-i\frac{\pi}{4}}\overset{+}{\delta}{}^{(-\frac{1}{2})}\right\}\right](t) \tag{C6}$$

where $\otimes$ stands for a convolution and the operator $\overset{+}{\delta}{}^{(-\frac{1}{2})}$ is defined via the analytic Fourier transform

$$\overset{+}{\delta}{}^{(-\frac{1}{2})}(t) \overset{\text{def}}{=} \frac{1}{\pi}\int_0^{\infty} d\omega \frac{e^{-i\omega t}}{\sqrt{-i\omega}} = \frac{1}{\sqrt{\pi t}}, \quad \mathrm{Im}\,(t) \le 0 \tag{C7}$$

and in the real t limit

$$\mathrm{Re}\left\{e^{-i\frac{\pi}{4}}\overset{+}{\delta}{}^{(-\frac{1}{2})}(t)\right\} = \frac{1}{\sqrt{2\pi\,|t|}} \quad t \text{ real.} \tag{C8}$$

Next, we note that the time argument in $\overset{+}{\Upsilon}{}^{(N-\frac{1}{2})}(t)$ is complex as follows from (C4), hence we should understand the convolution in (C6) between an analytic signal $\overset{+}{h}_1$ with complex t, $\mathrm{Im}\, t \le 0$ and a real signal h_2 for real t as

$$[\overset{+}{h}_1 \otimes h_2](t) = \int_{-\infty}^{\infty} dt'\, \overset{+}{h}_1(t-t')h_2(t'), \quad \mathrm{Im}\, t \le 0 \tag{C9}$$

where the integration is performed along the real t' axis. In view of (C8), the final expression for the fractional derivative in (C6) becomes

$$e^{-i\frac{\pi}{4}}\overset{+}{\Upsilon}{}^{(n-\frac{1}{2})}(t) = \int_{-\infty}^{\infty} dt'\, \overset{+}{\Upsilon}{}^{(n)}(t-t')\frac{1}{\sqrt{2\pi\,|t'|}} \tag{C10}$$

where t in $\overset{+}{\Upsilon}{}^{(n)}$ is in general complex with $\mathrm{Im}\, t \le 0$.

Finally, we discuss the effect of the parameters (γ, α), as was done after (B6) in the context of the 3-D formulation. Noting that the convolution with $1/\sqrt{|t|}$ in (C10) does not change the symmetry of the signal $\overset{+}{\Upsilon}{}^{(n)}(t)$ about $t = 0$, we find by substituting (C10) in (C5) and repeating the analysis done after (B6) that the structure of the PB is essentially the same as in the 3-D case, as summarized in Table I. The only difference is for $\Psi^{\pm}_{\boldsymbol{\mu},s}(\mathbf{r},t)$ in the far zone, where the argument of the square root in (C4) tends to $e^{-i\pi/4}$ rather than to $-i$ as in the 3-D case. It follows that the PB structure there is a balanced sum of symmetrical and antisymmetrical wavepackets.

References

[1] E. Heyman and L. B. Felsen, "Gaussian beam and pulsed-beam dynamics: Complex-source and complex-spectrum formulations within and beyond paraxial asymptotics," *J. Opt. Soc. Amer. A, Opt. Image Sci.*, vol. 18, no. 7, pp. 1588–1611, 2001.

[2] A. Shlivinski, E. Heyman, A. Boag, and C. Letrou, "A phase-space beam summation formulation for ultrawide-band radiation," *IEEE Trans. Antennas Propag.*, vol. 52, no. 8, pp. 2042–2056, Aug. 2004.

[3] M. J. Bastiaans, "Signal description by means of a local frequency spectrum," *Proc. SPIE*, vol. 373, Feb. 1984, pp. 49–62.

[4] B. Z. Steinberg, E. Heyman, and L. B. Felsen, "Phase-space beam summation for time-harmonic radiation from large apertures," *J. Opt. Soc. Amer. A, Opt. Image Sci.*, vol. 8, no. 1, pp. 41–59, 1991.

[5] J. J. Maciel and L. B. Felsen, "Gaussian beam analysis of propagation from an extended plane aperture distribution through dielectric layers. I. Plane layer," *IEEE Trans. Antennas Propag.*, vol. 38, no. 10, pp. 1607–1617, Oct. 1990.

[6] V. Galdi, L. B. Felsen, and D. A. Castañon, "Quasi-ray Gaussian beam algorithm for time-harmonic two-dimensional scattering by moderately rough interfaces," *IEEE Trans. Antennas Propag.*, vol. 49, no. 9, pp. 1305–1314, Sep. 2001.

[7] B. Z. Steinberg and E. Heyman, "Phase-space beam summation for time-dependent radiation from large apertures: Discretized parameterization," *J. Opt. Soc. Amer. A, Opt. Image Sci.*, vol. 8, pp. 959–966, 1991.

[8] D. Lugara and C. Letrou, "Alternative to Gabor's representation of plane aperture radiation," *Electron. Lett.*, vol. 34, no. 24, pp. 2286–2287, Nov. 1998.

[9] A. Shlivinski, E. Heyman, and A. Boag, "A pulsed beam summation formulation for short pulse radiation based on windowed Radon transform (WRT) frames," *IEEE Trans. Antennas Propag.*, vol. 53, no. 9, pp. 3030–3048, Sep. 2005.

[10] T. Melamed, "TE and TM beam decomposition of time-harmonic electromagnetic waves," *J. Opt. Soc. Amer. A, Opt. Image Sci.*, vol. 28, no. 3, pp. 401–409, 2011.

[11] T. Melamed, D. Abuhasira, and D. Dayan, "Transverse electric and transverse magnetic pulsed beam decomposition of time-dependent aperture fields," *J. Opt. Soc. Amer. A, Opt. Image Sci.*, vol. 29, no. 6, pp. 1115–1123, 2012.

[12] M. Leibovich and E. Heyman, "Beam summation theory for waves in fluctuating media. Part I: The beam frame and the beam-domain scattering matrix," *IEEE Trans. Antennas Propag.*, vol. 65, no. 10, pp. 5431–5442, Oct. 2017.

[13] M. Leibovich and E. Heyman, "Beam summation theory for waves in fluctuating media. Part II: Stochastic field representation," *IEEE Trans. Antennas Propag.*, vol. 65, no. 10, pp. 5443–5452, Oct. 2017.

[14] R. Tuvi, E. Heyman, and T. Melamed, "Propagating beam frame: A novel formulation for time-dependent radiation and scattering," in *Proc. Int. Symp. Electromagn. Theory*, Espoo, Finland, Aug. 2016, pp. 169–172.

[15] R. Tuvi, E. Heyman, and T. Melamed, "Propagating beam frame: A novel formulation for local inverse scattering," in *Proc. 32nd Gen. Assem. Sci. Symp. Int. Union Radio Sci. (URSI)*, Montreal, QC, Canada, Aug. 2017, pp. 1–4.

[16] R. Tuvi, E. Heyman, and T. Melamed, "UWB beam-based local diffraction tomography. Part I: Phase-space processing and physical interpretation," *IEEE Trans. Antennas Propag.*, submitted for publication.

[17] R. Tuvi, E. Heyman, and T. Melamed, "UWB beam-based local diffraction tomography. Part II: The inverse problem," *IEEE Trans. Antennas Propag.*, submitted for publication.

[18] R. Tuvi, "Beam-based local tomographic inverse scattering," Ph.D. dissertation, Tel Aviv Univ., Tel Aviv-Yafo, Israel, Dec. 2018.

[19] E. Heyman, "Pulsed beam propagation in inhomogeneous medium," *IEEE Trans. Antennas Propag.*, vol. 42, no. 3, pp. 311–319, Mar. 1994.

[20] E. Heyman, "Pulsed beam solutions for propagation and scattering problems," in *Scattering: Scattering and Inverse Scattering in Pure and Applied Science*, vol. 1, R. E. Pike and P. C. Sabatier, eds. New York, NY, USA: Academic, 2002, ch. 1.5.4, pp. 295–315.

[21] T. Heilpern, E. Heyman, and V. Timchenko, "A beam summation algorithm for wave radiation and guidance in stratified media," *J. Acoust. Soc. Amer.*, vol. 121, pp. 1856–1864, 2007.

[22] E. Heyman, "Time-dependent plane-wave spectrum representations for radiation from volume source distributions " *J. Math. Phys.*, vol. 37, no. 2, pp. 658–681, 1996.

[23] E. Heyman and T. Melamed, "Space-time representation of ultra wideband signals," in *Advances in Imaging and Electron Physics*, vol. 103. New York, NY, USA: Academic, 1998, pp. 1–63.

[24] Y. Gluk and E. Heyman, "Pulsed beams expansion algorithms for time-dependent point-source radiation. A basic algorithm and a standard-pulsed-beams algorithm," *IEEE Trans. Antennas Propag.*, vol. 59, no. 4, pp. 1356–1371, Apr. 2011.

Ram Tuvi was born in Holon, Israel, in 1982. He received the B.Sc. and M.Sc. *(cum laude)* degrees in electrical and computer engineering from the Ben-Gurion University of the Negev, Beersheba, Israel, in 2010 and 2013, respectively. He is currently pursuing the Ph.D. degree with the Department of Physical Electronics, School of Electrical Engineering, Tel Aviv University, Tel Aviv, Israel.

His current research interests include electromagnetics, wave theory, scattering, and inverse scattering.

Ehud Heyman (S'80–M'82–SM'88–F'01–LF'17) was born in Tel Aviv, Israel, in 1952. He received the B.Sc. degree *(summa cum laude)* in electrical engineering from Tel Aviv University, Tel Aviv, Israel, the M.Sc. degree in electrical engineering (Hons.) from the Technion—Israel Institute of Technology, Haifa, Israel, and the Ph.D. degree in electrophysics from the Polytechnic Institute of New York (Brooklyn Polytech), Brooklyn, NY, USA, in 1977, 1979, and 1982, respectively.

He was a Rothschild Fellow, a Fullbright Fellow, and a Hebrew Technical Institute Fellow with the Polytechnic Institute of New York. In 1983, he joined the Department of Physical Electronics, Tel Aviv University, where he is currently a Professor and the incumbent of the Jokel Chair of Electromagnetics. He served as the Founding Head of the School of Electrical Engineering from 2002 to 2005, and the Dean of Engineering from 2005 to 2014. He has authored or co-authored over 120 refereed journal articles, and has been an Invited Speaker at many international conferences. His current research interests include analytic methods in wave theory, including asymptotic and time-domain techniques for propagation and scattering, beam and pulsed-beam techniques, short-pulse antennas, inverse scattering, target identification, imaging and synthetic aperture radar, and propagation in random medium.

Dr. Heyman is a member of Sigma Xi and the Chairman of the Israeli National Committee for Radio Sciences (URSI). He was a recipient of the Balthasar van der Pol Gold Medal Award of URSI for the year 2011. He was an Associate Editor of the *IEEE Press Series on Electromagnetic Waves* and the IEEE TRANSACTIONS ON ANTENNAS AND PROPAGATION.

Timor Melamed (M'99–SM'01) was born is Tel Aviv, Israel, in 1964. He received the B.Sc. degree *(magna cum laude)* in electrical engineering and the Ph.D. degree from Tel Aviv University, Tel Aviv, in 1989 and 1996, respectively.

From 1996 to 1998, he held a postdoctoral position with the Department of Aerospace and Mechanical Engineering, Boston University, Boston, MA, USA, and collaborated with Prof. L. B. Felsen. He is currently with the Department of Electrical and Computer Engineering, Ben-Gurion University of the Negev, Beersheba, Israel. His current research interests include propagation and scattering of waves, analytical methods in the time domain, scattering from moving objects, and beam methods.